Landers 1992 "reloaded": an integrative dynamic earthquake rupture model

Corresponding author: Stephanie Wollherr (wollherr@geophysik.uni-muenchen.de)

Stephanie Wollherr[1], Alice-Agnes Gabriel[1], and P. Martin Mai[2]

[1]Department of Earth and Environmental Sciences, Ludwig-Maximilians-University, Munich, Germany
[2]Division of Physical Science and Engineering, King Abdullah University of Science and Technology, Thuwal, Kingdom of Saudi Arabia

Key Points:

- A new integrative physics-based simulation of the 1992 Landers earthquake reproduces a broad range of independent observation
- Sustained dynamic rupture interconnecting the complex fault segments constraints pre-stress and fault strength
- We discuss the interplay of rupture transfers, geometric fault complexity, initial stress, viscoelastic attenuation, and off-fault plasticity

Corresponding author: Stephanie Wollherr, wollherr@geophysik.uni-muenchen.de

Abstract

The 1992 M_w 7.3 Landers earthquake is perhaps one of the best studied seismic events. However, many aspects of the dynamics of the rupture process are still puzzling, e.g. how did rupture transfer between fault segments? We present 3D spontaneous dynamic rupture simulations of a new degree of realism, incorporating the interplay of fault geometry, topography, 3D rheology, off-fault plasticity and viscoelastic attenuation. The surprisingly unique scenario reproduces a broad range of observations, including final slip distribution, seismic moment-rate function, seismic waveform characteristics and peak ground velocities, as well as shallow slip deficits and mapped off-fault deformation patterns. Sustained dynamic rupture of all fault segments in general, and rupture transfers in particular, put strong constraints on amplitude and orientation of initial fault stresses and friction. Source dynamics include dynamic triggering over large distances and direct branching; rupture terminates spontaneously on most of the principal fault segments. We achieve good agreement between synthetic and observed waveform characteristics and associated peak ground velocities. Despite very complex rupture evolution, ground motion variability is close to what is commonly assumed in Ground Motion Prediction Equations. We examine the effects of variations in modeling parameterization, e.g. purely elastic setups or models neglecting viscoelastic attenuation, in comparison to our preferred model. Our integrative dynamic modeling approach demonstrates the potential of consistent in-scale earthquake rupture simulations for augmenting earthquake source observations and improving the understanding of earthquake source physics of complex, segmented fault systems.

1 Introduction

The M_w 7.3 Landers earthquake of June 28, 1992 ruptured five distinct segments previously considered unconnected. Overlapping fault zones of 80 km length hosted large vertical slips, large surface strike-slip offsets and unusual high stress-drops [*Kanamori et al.*, 1992; *Sieh et al.*, 1993]. Only two segments of the strike-slip fault system slipped over their respective total length, the previously unknown Kickapoo fault and the Homestead Valley fault (Fig. 1), while only parts of the other involved fault segments ruptured. The Landers event raised awareness of unexpectedly large magnitude earthquakes hosted by complicated fault networks; in particular the dynamic rupture transfer mechanisms which pose pressing questions of fault mechanics. Distinct ground shaking was recorded by a dense network of seismometers [*Campbell and Bozorgnia*, 1994] including locations very close to the slipping faults [*Chen*, 1995; *Sleep*, 2012].

The wealth of observational data has been analyzed to shed light on the slip distribution from inversion of seismological and geodetic data [e.g., *Wald and Heaton*, 1994; *Cohee and Beroza*, 1994; *Freymueller et al.*, 1994; *Cotton and Campillo*, 1995; *Fialko*, 2004a; *Xu et al.*, 2016] and to constrain rupture dynamics [e.g. *Peyrat et al.*, 2001; *Aochi and Fukuyama*, 2002; *Fliss et al.*, 2005; *Heinecke et al.*, 2014; *Wollherr et al.*, 2018]. Together with detailed analysis of the recorded strong ground motions [e.g., *Campbell and Bozorgnia*, 1994], rupture transfer mechanisms [e.g., *Wesnousky*, 2006; *Madden and Pollard*, 2012; *Madden et al.*, 2013] and potential energy release [e.g., *Dreger*, 1994; *Wald and Heaton*, 1994] a comprehensive picture of the source kinematics and macroscopic earthquake properties has been developed.

While the overall kinematics of the event are thought to be well understood, many observations regarding its complicated rupture dynamics are still unresolved. For instance, the Kickapoo-Landers fault unexpectedly connected the Johnson Valley fault and the Homestead Valley fault, which were previously assumed to be independent structures [*Sowers et al.*, 1994]. A well-recorded near-surface slip gap at the northern part of the Kickapoo fault, close to the junction to the Homestead Valley fault, suggests a disconnection between these faults. Thus, rupture is assumed to have propagated at depth and/or "jumped" via dynamic triggering to the adjacent fault segment [*Spotila and Sieh*, 1995]. Across the entire fault system, the rupture front is found to propagate at highly variable speeds [*Cotton and Campillo*, 1995; *Hernandez et al.*, 1999], slowing down at transitions between segments [*Wald and Heaton*, 1994] and in regions of high slip [*Cohee and Beroza*, 1994].

The orientation of geometrically complex faults in the tectonic stress field has a first-order impact on the mechanics of earthquakes and faulting [e.g., *Kaven and Pollard*, 2013]. The Landers fault geometry is characterized by nearly vertical dip but exhibits strike rotation by about 30° from its original direction of nucleation [*Bouchon and Campillo*, 1998]. Of particular interest is the fact that the northern fault segments, including the Emerson fault and Camp Rock fault, are not well oriented with respect to the regional stress field, indicating locally higher fault strengths and lower initial shear stresses. This leads to the hypothesis that large dynamic stress changes induced by rupture of the adjacent fault segments are necessary to overcome static friction at the northernmost faults [*Bouchon and Campillo*, 1998]. In contrast, the lack of aftershocks and large fault offsets in conjunction with relatively shallow slip [*Wald and Heaton*, 1994], suggests that the Camp Rock fault was rather statically triggered shortly after the event [*Sieh*, 1996; *Kaneda and Rockwell*, 2009].

Physics-based dynamic rupture simulations allow investigating the full complexity of the earthquake source dynamics by numerically modeling a spontaneously propagating rupture on a prescribed fault surface. The space-time evolution of the rupture is thereby governed by initial stresses on the fault, a frictional constitutive law, and

the bulk properties of the medium. *Olsen et al.* [1997] presents the first dynamic rupture model of the Landers event using a single planar fault and initial stresses derived from the slip distribution of *Wald and Heaton* [1994]. Consequently, their model features very heterogeneous on-fault stress conditions. This model is then subsequently refined in an iterative dynamic rupture inversion approach [*Peyrat et al.*, 2001] and well reproduces recorded seismograms at selected sites for frequencies below 0.5 Hz.

However, simulations on single planar faults provide no insight on rupture transfer between fault segments. Also, rupture nucleation, propagation and arrest are highly sensitive to variations in fault geometry. Dynamically, rupture is able to overcome fault bends, branch into or jump to adjacent fault segments only for specific fault pre-stresses, limited distances between adjacent fault segments and limited branching angles of connected faults [e.g., *Harris and Day*, 1993; *Bhat et al.*, 2007; *Oglesby*, 2008; *Lozos et al.*, 2011; *DeDontney et al.*, 2012; *Oglesby and Mai*, 2012].

Modeling complex fault geometries is challenging for numerical solvers, since the detailed geometry must be honored explicitly by the spatial discretization. Numerical schemes such as the Boundary Integral Equation Method (BIEM) [e.g., *Aochi and Fukuyama*, 2002; *Ando et al.*, 2017], Finite Element Methods (FEM) based on tetrahedral elements [e.g., *Barall*, 2009] - including the Discontinuous Galerkin (DG) Method [e.g., *Pelties et al.*, 2012; *Tago et al.*, 2012] - or numerical methods using curvilinear elements [e.g., *Duru and Dunham*, 2016] are able to accurately represent non-planar fault geometries. We point out that the accurate representation of fault branches is restricted to methods that do not use a traction-at-split nodes approach [*Andrews*, 1999; *Day et al.*, 2005; *Dalguer and Day*, 2007], like BIEM and DG methods.

Only a few dynamic rupture scenarios considered the complex fault geometry on which the Landers event occurred. A multi-segment geometry of the Landers fault zone is first integrated into a dynamic rupture model by *Aochi and Fukuyama* [2002] and *Aochi et al.* [2003]. By analyzing the effects of varying principal stress directions and frictional parameters they conclude that rupture cannot propagate across all of the differently oriented fault segments assuming a single principal stress orientation. That is, the local tectonic setting and non-planar fault structure play the most significant role in this earthquakes generation and rupture process. However, the use of the BIEM restricted this study to fully elastic, homogeneous material properties. Additionally, the Landers earthquake serves as valuable validation and testing scenario, for example for demonstrating the geometrical flexibility of DG methods [*Tago et al.*, 2012; *Pelties et al.*, 2012; *Breuer et al.*, 2014]. However, these studies are not able to fully reproduce observations, as e.g. slip on all fault segments or regional seismogram recordings. While these studies incorporate realistic fault geometries and topography, realistic material properties, such as 3D subsurface structure and the possibility of plastic deformation, are missing.

In addition, significant fault-zone damage was observed for the Landers earthquake [e.g., *Li et al.*, 1994a,b], motivating us to account for inelastic processes off the fault. Recent advances in processing high-resolution aerial photographs of near-fault deformation patterns reveal that off-fault deformation primarily correlates with fault complexity [*Milliner et al.*, 2015]. A significant slip reduction towards the shallow part of the faults is inferred, known as shallow slip deficit (SSD), which is often attributed to plastic deformation [*Fialko et al.*, 2005; *Kaneko and Fialko*, 2011; *Milliner et al.*, 2015; *Gombert et al.*, 2018]. Simulations on a single, planar fault plane reveal that purely elastic simulations underpredict the SSD [*Roten et al.*, 2017] as well as ground motions [*Roten et al.*, 2014, 2015]. *Wollherr et al.* [2018] includes the full geometrical complexity of the fault system in scenario calculations demonstrating that spatio-temporal rupture transfers are significantly altered by off-fault plasticity.

In this study, we develop an integrated dynamic source model for the the multi-segment Landers earthquake based on physics-based and high-performance-computing-enabled rupture simulations. Our dynamic source model incorporates new degree of realism by integrating a comprehensive set of geological and geophysical information such as high-resolution topography, rotating tectonic stresses, 3D velocity structure, depth-dependent bulk cohesion, and a complex intersecting fault geometry. Unifying aforementioned complexities is enabled by using SeisSol (`www.seissol.org`, *Dumbser and Käser* [2006]; *Pelties et al.* [2014]), a software package specifically suited for handling complex geometries and for the efficient use on modern high-performance computing infrastructure [e.g., *Heinecke et al.*, 2014; *Uphoff et al.*, 2017]. This work extends recent models presented in [*Heinecke et al.*, 2014; *Wollherr et al.*, 2018] which included complex fault geometries and off-fault plasticity but were restricted to 1D velocity structure, constantly oriented tectonic background stress and neglecting viscoelastic attenuation of the seismic wave field.

We find that the interplay of dynamic rupture transfers, geometric fault complexity, spatially smoothly varying pre-stress, 3D velocity structure, topography, viscoelastic attenuation and off-fault plasticity pose unique conditions for a mechanically self-consistent dynamic source model. The such constrained simulation matches a broad range of regional and local observations, including fault slip, seismic moment release and ground motions. The presented model also contributes to the understanding of the shallow slip deficit, directivity effects and rupture branching and "jumping" under realistic conditions.

In the following, we first describe our modeling approach and the observational constraints considered. We then investigate the rupture characteristics of our preferred model in terms of rupture branching, dynamic triggering, moment-rate release, and final slip distribution in Sec. 3. We compare the ratio of shallow near-surface slip and deep slip (within the seismogenic zone) to recent inversion results based on a Bayesian approach [*Gombert et al.*, 2018], as well as the modeled off-fault plastic strain distribution with near-field observations of fault zone width [*Milliner et al.*, 2015]. Analyzing ground motions in terms of spatial distribution and shaking levels (e.g. peak ground motions) with respect to the observations proves an excellent quality of the synthetics produced by the dynamic rupture model. We lastly discuss the effects of variations in modeling parameterization, e.g. purely elastic setups or models neglecting viscoelastic attenuation, in comparison to our preferred model, as well as implications for understanding earthquake dynamics on segmented fault systems in Sec. 4.

2 Model

In the following, we describe our modeling approach and the observational constraints to construct a fully self-consistent dynamic rupture model of the 1992 Landers earthquake. Dynamic rupture evolves spontaneously according to the parameterization of frictional behavior, initial fault stress state, and nucleation conditions on prescribed fault surfaces. The nonlinear interaction of rupture propagation and the emanated seismic wave field is further affected by the structural characteristics, such as material properties and topography of the modeling domain.

To construct our reference model, we follow a well-defined sequence in order to optimize the model parametrization in terms of stress-to-fault angles, stress amplitudes, and frictional parameters under the given fault geometry, velocity structure, off-fault plasticity parametrization and vertical stress amplitudes. The model refinement steps outlined below allows us to create a dynamic rupture model that reproduces a broad range of independent observations.

1. **Sustained rupture along all fault segments:** The assumption of sustained rupture along all fault segments assuming a regional stress state without small scale heterogeneities governing across complex fault geometries introduces strong constraints on the choice of modeling parameters. By carefully testing a range of horizontal stress orientations (i.e. the angle of the regional maximum compressive stress orientation with respect to the fault system) based on inferences from the geological setting and previous seismicity (more details in Sec. 2.2), we constrain the stress orientations in the range of a few degrees variance to the preferred model.
2. **Seismic moment:** We aim to find a model parametrization that leads to a scenario with a seismic moment comparable to the observationally inferred seismic moment. Criterion 2 constraints the stress amplitudes and the frictional parameters to narrow range.
3. **Peak seismic moment release:** In this step, we simultaneously vary the stress orientations within the few degree variance identified in step 1 together with the frictional parameters of the friction law. We aim to match the peak amplitudes of moment rate release of the synthetic seismic moment rate release with observationally estimated source time functions. The misfit in terms of amplitudes is measured by an envelope goodness-of-fit criteria based on the frequency-time (TF) representation of the signal following *Kristeková et al.* [2009].
4. **Timing of the peak seismic moment release:** Lastly, we optimize the phase alignment and timing of the moment release (quantified by the phase goodness-of-fit criteria defined by *Kristeková et al.* [2009] and determine the final frictional parameters, in particular the critical slip distance of the friction law.

We detail the time-frequency goodness-of-fit criteria used in step 3 and 4 exemplarily for selected models in the supporting information (Text S1 and Fig. S1, calculated using ObsPy [*Krischer et al.*, 2015].). The such constrained model is presented in the following including a summary of all model parameters in Table 1. It captures the interplay of dynamic rupture transfers, geometric fault complexity, spatially smoothly varying pre-stress, 3D velocity structure, topography, viscoelastic attenuation, and off-fault plasticity under unique preferred conditions for a mechanically self-consistent dynamic source model.

2.1 Structural Model and Numerical Discretization

The Landers fault system consists of curved, branched, and segmented faults. We construct the geometry of the main fault segments from photometric images of fault surface traces [*Fleming et al.*, 1998] that we extend to 15 km depth assuming

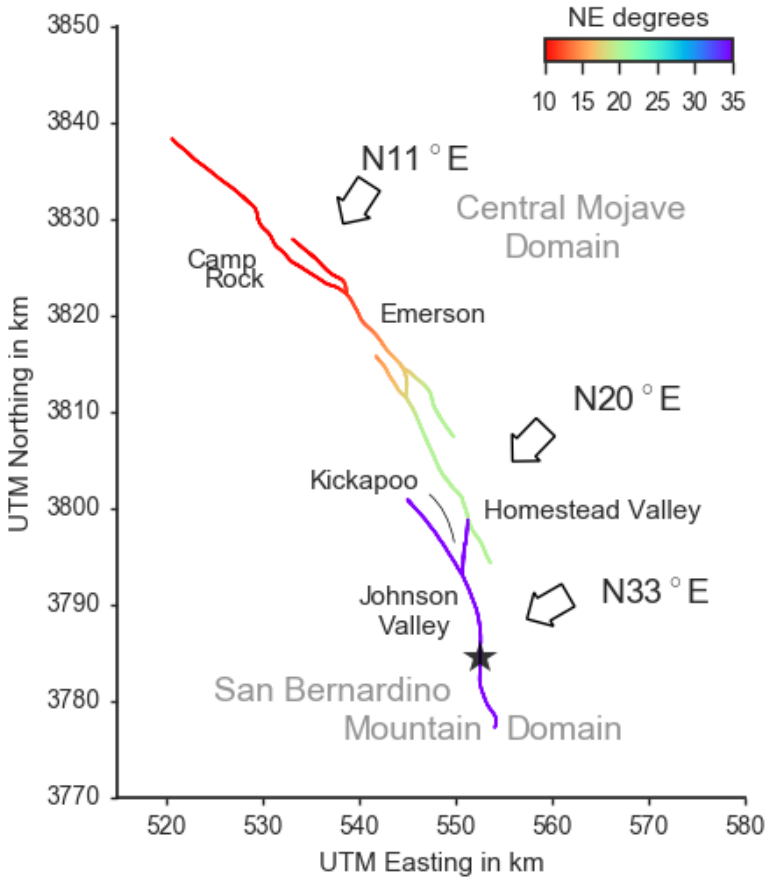

Figure 1. Mapped fault traces [*Fleming et al.*, 1998] that are used in our model and assumed orientation of maximum compressional principal stress σ_1. The star marks the epicenter of the 1992 M_w 7.3 Landers earthquake.

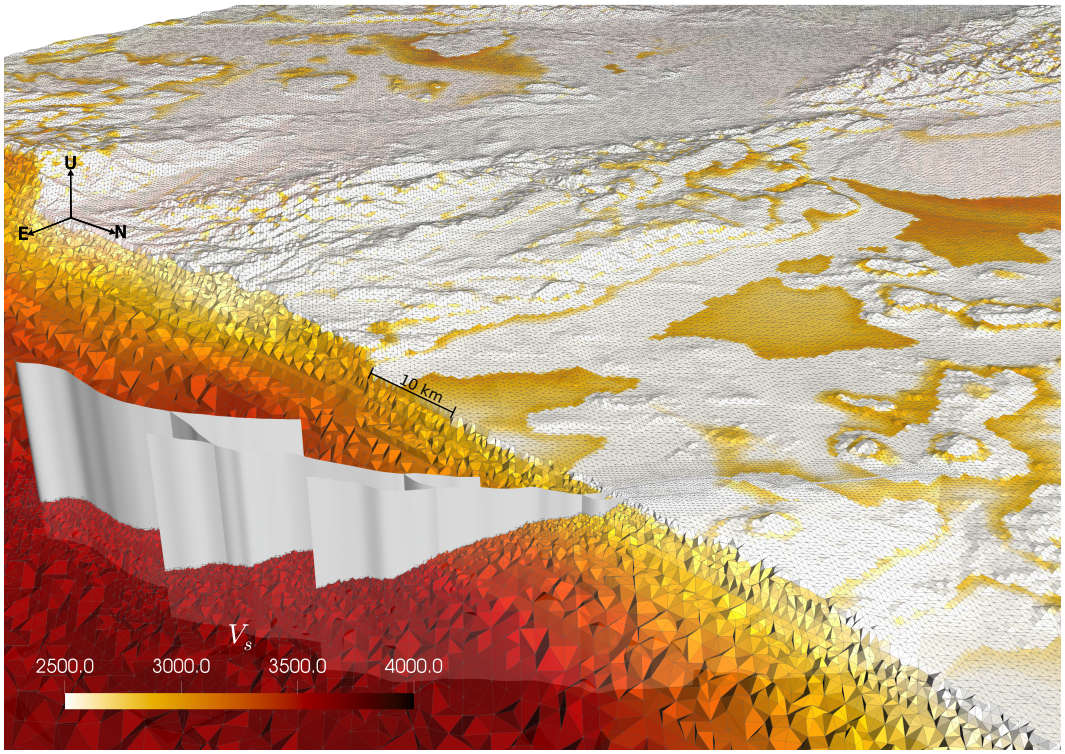

Figure 2. Structural model spatially discretized by tetrahedral computational elements. Colors represent the shear wave velocities V_s of the 3D velocity structure given by the Community Velocity Model-Harvard (CVM-H) [*Shaw et al.*, 2015]. Fault surface segments are visualized in white. Local refinement is applied in the vicinity of the faults (200 m) [*Fleming et al.*, 1998] and the Earth's topography (500 m) [*Farr et al.*, 2007]. The fault surfaces intersect the local topography.

symbol	parameter	value with units
μ_s	static friction	0.55 (0.44 at the EF and CRF)
μ_d	dynamic friction	0.22
D_c	critical slip distance	0.62 m
c	bulk cohesion	depth-dependent, good quality rock model of *Roten et al.* [2017], ranging between 2.5–50.0 MPa
ϕ	friction angle	0.55
v_s, v_p	shear and p-wave velocity	3D CVM-H [*Shaw et al.*, 2015]
ρ	density	3D CVM-H [*Shaw et al.*, 2015]
Q_s, Q_p	viscoelastic damping parameters	50 v_s, 2 Q_s
r	nucleation patch radius	1.5 km
	forced nucleation time	0.5 s
R	relative pre-stress ratio	0.65
σ_2	principal vertical stress	(2700 – 1000) kg/m 9.8 abs(depth m)
σ_1, σ_3	principal horizontal stresses	orientation visualized in Fig. 1, amplitudes determined by R and eq. (2) and (3)
dx	smallest element edge	200 m
p	polynomial order of accuracy	4

Table 1. Summary of the model parameters of the reference model described in Secs. 2.1 – 2.5.

purely vertical dip. The model includes five distinct non-planar fault segments connected over a total length of 80 km (see Fig. 1): the Johnson Valley fault (JVF) in the most southern part of the fault system, the Kickapoo fault (KF) connecting to the Homestead Valley fault (HVF), the Emerson fault (EF) including the connecting branch between the HVF and EF, and the Camp Rock fault (CRF) in the northernmost part. The fault surface intersects the local topography, leading to fault elevation differences of up to 1000 m. Our model incorporates DEM data of NASA's Shuttle Radar Topography Mission (SRTM) with 3-arc-seconds sampling (available from the U.S. Geological Survey `https://dds.cr.usgs.gov/srtm/version2_1/SRTM3/`,([*Farr et al.*, 2007])), re-sampled to match a here chosen spatial topography discretization of 500 m. A cutout of the resultant structural model is visualized in Fig. 2.

In *Wollherr et al.* [2018] it was found that the cohesive zone width may vary considerably across geometrically complex fault systems, implying that a minimum intrinsic scale length needs to be resolved instead of some average. For our preferred scenario, we measure a minimum cohesive zone width of 155 m, located at the HVF at a depth of 8 km. Following the convergence tests conducted in *Wollherr et al.* [2018], a fault discretization of 200 m using polynomial basis functions of degree $p = 4$ or $\mathcal{O}5$ (corresponding to a minimum cohesive zone resolution of 0.78 mesh elements or 3.88 subelemental points due to the high-order approach) sufficiently resolves the cohesive zone width to ensure convergence defined by *Day et al.* [2005]. Due to the use of sub-elemental Gaussian integration points, the fault is efficiently discretized by a maximum distance of 33.3 m (effective minimum cohesive zone width resolution of 4.65 points). More details on the determination of the cohesive zone width and the required resolution are provided in the Appendix A: .

We define a high-resolution model area surrounding the fault traces over a width and length of 270 km (east-west and north-south, respectively). Within this area, topography is represented by tetrahedral elements with 500 m edge length (Fig. 2). Based on the locally refined and high-order spatio-temporal discretization, we resolve

a maximum of 1.0 Hz in all analyzed synthetic waveforms in Sec. 3.5 within 105 km distance to the fault trace. Synthetic measurements in the vicinity of low velocity basins resolve up to 1 Hz, while high frequencies up to 4.0 Hz are resolved within 10 km distance to the fault trace. Fig. B.1 in Appendix B illustrates the model's resolution exemplary for several stations with varying distances to the fault trace ranging from 0.47 km (station LUC) to 102.8 km (station SAL located on the Salton Sea Basin).

To avoid undesired reflections from the domain boundaries, while simultaneously saving computational costs, we gradually increase the element size by a factor of 6% from element to element up to an edge length of 10 km outside the high-resolution model area. Equivalent mesh-coarsening is applied in the volume at depth.

2.2 On-fault Initial Stresses

To constrain the initial stress conditions, we combine information on the regional tectonic setting, findings of previous dynamic rupture studies, and newly conducted numerical experiments constraining the principal stress directions.

Principal stresses are assumed to vary linearly with depth, in accordance with rock mechanics and field observations. Our prescribed intermediate principal stress component, σ_2, is purely vertical and set to the average confining pressure of the overlying rock reduced by a constant hydrostatic pore fluid pressure [e.g., *Suppe*, 1985], i.e.

$$\sigma_2 = (2700 - 1000)\mathrm{kg/m^3}\ gz \tag{1}$$

with gravity $g = 9.8$ m/s^2, average rock density of 2700 kg/m^3, and depth z in m. We further follow [*Aochi and Madariaga*, 2003] and assume $\sigma_2 = (\sigma_1 + \sigma_3)/2$ and $\Delta\sigma = (\sigma_1 - \sigma_3)/2$ where $\Delta\sigma$ defines the radius of the corresponding Mohr-Coulomb stress circle. As a consequence the horizontal stresses can be represented as $\sigma_1 = \sigma_2 + \Delta\sigma$ and $\sigma_3 = \sigma_2 - \Delta\sigma$. Using these definitions we can derive the initial shear and normal stress in dependence of $\Delta\sigma$ for a fault plane with orientation ϕ:

$$\begin{aligned} \tau^0 &= \Delta\sigma \sin(2\phi) \\ \sigma_n^0 &= \sigma_2 - \Delta\sigma \cos(2\phi). \end{aligned} \tag{2}$$

For given static and dynamic friction coefficient μ_s and μ_d, and given frictional cohesion c, the relative pre-stress R-ratio as defined by [*Aochi and Madariaga*, 2003] is defined as the fault stress drop $\Delta\tau$ over breakdown strength drop $\Delta\tau_b$:

$$R = \frac{\Delta\tau}{\Delta\tau_b} = \frac{\tau^0 - \mu_d\sigma_n^0}{c + \mu_s\sigma_n^0 - \mu_d\sigma_n^0}. \tag{3}$$

By inserting τ^0 and σ_n^0 from eq. 2 into eq. 3 we derive $\Delta\sigma$ and hence the magnitude of the horizontal principal stresses σ_1 and σ_3. Specifically, we strive to uniquely determine the horizontal principal stress amplitudes such that the stress field is most favorably oriented at the hypocenter [*Ulrich et al.*, 2018], ensuring that the thus optimally oriented fault plane reaches failure before any other fault with different orientation.

The relative level of initial stress has been found to determine rupture style and rupture properties [e.g., *Dunham*, 2007; *Gabriel et al.*, 2012, 2013]. The described R ratio is related to the commonly used S value [e.g., *Das and Aki*, 1977] as $S = 1/R - 1$. In our simulations, we assume $R = 0.65$ which leads to a potential stress drop of 65% of the breakdown strength drop across the entire fault. Numerical experiments, testing R-ratios in the range of $0.5 < R < 0.9$ and different horizontal stress orientations as described below, reveal that $R = 0.65$ optimally balances reasonable values of rupture

speed and final slip while sustaining rupture across all fault segments by facilitating rupture transfers.

The chosen R value corresponds to a low S value of 0.54 value indicating a rather weak fault. We note, that geometric complexity, the 3D Earth model and partially visco-elasto-plasticity prevent the occurrence of sustained supershear rupture in our preferred scenario. Conditions of apparent fault weakness were recently found to promote rupture cascading in dynamic rupture models along complex faults [*Ulrich et al.*, 2018].

In terms of horizontal stress orientations, the state of stress governing the Landers main shock is only incompletely known due to limited direct measurements of crustal stress in the Mojave block of the Eastern California Shear Zone. The region is characterized by north-west trending strike-slip faulting and a principal stress orientation of approximately N20°E [*Nur et al.*, 1989; *Hauksson*, 1994]. The Mojave block can be subdivided into several distinct domains based on geometry and faulting style of tectonic activity [e.g., *Dokka and Travis*, 1990; *Unruh et al.*, 1994]. While the central and northern part of the fault system (i.e. HVF, EF and CRF) belongs to the central Mojave block, *Unruh et al.* [1994] suggest that the JVF forms the eastern boundary of a distinct domain around the San Bernardino Mountains characterized by more north-striking strike slip faults.

To understand the details of the dynamic rupture process, the principal stress orientations across the Landers fault system are particularly important. Focal-mechanism analysis of the 1975 Galway and the 1979 Homestead Valley earthquakes, as well as of background seismicity prior to the 1992 Landers main shock, yields a maximum principal stress angle of 38° to 16° NE [*Hauksson*, 1994]. That is, the inferred principal stress directions slightly rotate northwards up to the EF.

While background seismicity is mainly observed in the southern part of the fault system, little is known about the stress state prior the Landers earthquake of the northernmost segments [*Hauksson et al.*, 1993]. On the northern Landers fault system, an even steeper oriented maximum principal stress might be plausible, given the locally considerable higher maximum shear-strain orientation compared to the southern fault segments [*Sauber et al.*, 1986]. *Aochi and Fukuyama* [2002] hypothesize a northern rotation to steep angles based on the dynamically locked CRF in their simulations assuming a maximum principal stress orientation of N22°E. A steep angle of 11° NE enabled full dynamic rupture also of the northernmost segments under a non-rotating, depth-dependent background stress [*Heinecke et al.*, 2014; *Wollherr et al.*, 2018].

In this study, we allow for smoothly varying directions of maximum principal stress, consistent with regional stress estimates (summarized in Fig. 1), without any small-scale or randomized heterogeneities. The following model parameters are obtained by the model validation steps detailed at the beginning of Sec. 2. We find that in particular sustained rupture along and dynamic transfers in between fault segments pose the largest constraints on the horizontal stress field orientation.

As a result of our modeling workflow, we assume that the southern part of the fault system is contained in the San Bernardino Mountains domain [*Aochi and Fukuyama*, 2002; *Unruh et al.*, 1994], whereas all other fault segments are considered part of the central Mojave block. Therefore, in the south we prescribe a maximum principal stress orientation of N33°E governing the JVF and KF. The maximum principal stress orientation changes to 20° between the KF and the HVF [*Hauksson*, 1994]. We then smoothly decrease the principal stress direction northwards from N20°E at the HVF, consistent with the observed stress rotation postulated by *Hauksson* [1994].

Due to limited prior information, we perform several numerical experiments varying the principal stress orientation governing the CRF. We find that the CRF is orien-

tated very unfavorably under any angle between 15° and 38°. However, this segment ruptured with a substantial amount of slip [*Kagan and Houston*, 2005]. Sustained rupture across the EF and CRF occurs in our model under a locally low angle of maximum principal stress orientation of 11°, consistent with previous static and dynamic modeling studies of the full or southern-central fault system [*Madden et al.*, 2013; *Heinecke et al.*, 2014; *Wollherr et al.*, 2018].

While the prescribed stress field orientation is laterally smooth, the varying fault strike orientation generates a heterogeneous initial stress state across all fault segments, leading to both favorably and misaligned portions of the fault system. The Kickapoo branch and the northern part of the HVF are the most favorably orientated segments. In contrast, the northernmost part of JVF, as well as the northernmost and southernmost parts of the EF and CRF are not well aligned with respect to the regional principal stress orientation. As a consequence, these fault segments experience only marginal or no slip (see Sec. 3.2).

2.3 Frictional Properties

All frictional parameters are chosen constant across the fault system. Exceptions are the nucleation zone and the northernmost part of the fault system, where we account for palaeoseismological evidence.

Based on theoretical and numerical models of shear crack propagation [e.g., *Ida*, 1972] we use linear slip-weakening friction. We choose a static friction coefficient μ_s = 0.55 close to Byerlee's coefficient which is consistent with regional stress inversions [*Gross and Kisslinger*, 1997]. Under linear slip-weakening friction, a high stress drop is required to facilitate rupture transition between distinct fault segments. Based on our workflow, we find a dynamic coefficient of friction of $\mu_d = 0.22$ to optimally facilitate rupture cascading. Frictional cohesion c is set to 2 MPa for the entire fault system. The resulting average stress drop over all positive slip regions is approximately 12.5 MPa with a maximum stress drop of 33 MPa at 8 km depth. Surprisingly high stress drops were found for the Landers earthquake from energy to moment rate ratios [*Kanamori et al.*, 1992; *Sieh et al.*, 1993] and also agree with what is inferred from kinematic stress inversion [*Bouchon and Campillo*, 1998].

We observe a strong trade-off between rupture speed and critical slip distance D_c denoting the amount of slip over which friction drops from μ_s to μ_d. The critical slip distance also crucially affects rupture transitions by determining a critical nucleation size required to initiate spontaneous rupture via dynamic triggering. Step 4 of our modeling workflow reveals that $D_c = 0.62$ m ensures a balance of efficient rupture transfer between adjacent faults (in accordance with the moment rate release) and the prevention of pronounced supershear rupture.

While previous dynamic rupture simulations of the Landers earthquake choose D_c in the range of 0.8 m [*Olsen et al.*, 1997; *Peyrat et al.*, 2001], we find that lower D_c is required to sustain rupture across the here geometrically more complex fault system. Besides geometric effects, a lower D_c can be attributed to the effect of off-fault plasticity [*Roten et al.*, 2017; *Wollherr et al.*, 2018].

Paleoseismological evidences point to a large event occurring at the EF and CRF approximately 2000–3000 years ago, while the southern part of the fault system has not failed for 8000–9000 years [*Sieh*, 1996]. This suggests locally lower fault strengths due to not yet recovered static friction or lower regional stresses due to the more recent stress release. While we choose a constant stress ratio across the entire fault zone, we locally decrease fault strength by choosing $\mu_s = 0.44$ instead of 0.55 at the EF and the CRF segments. Our simulations reveal that slightly weakening the CRF and EF is crucial to facilitate dynamically triggered initiation of rupture on these segments which

also increases the fit with the observationally inferred seismic moment rate (step 4 of our modeling workflow).

Rupture is initiated using a artificial nucleation procedure within a circular patch of a 1.5 km radius. Within this zone, the friction coefficient is gradually reduced from its static to its dynamic value over a specified time of 0.5 s [*Bizzarri*, 2010]. Outside this zone, forced rupture is smoothly overtaken by spontaneous rupture. The hypocentral depth is set to 7 km as constrained by source inversion [*Wald and Heaton*, 1994; *Cotton and Campillo*, 1995; *Hernandez et al.*, 1999].

At depth, we account for the transition from the brittle to ductile regime between -9 km to -15 km. We linearly increase dynamic friction gradually up to static friction values which allows rupture to stop smoothly. By increasing fault strength instead of pre-stress with depth we ensure off- and on-fault stresses are equal which is necessary when accounting for off-fault plasticity.

2.4 Bulk Properties and Plasticity

Our model incorporates the 3D velocity structure of the Community Velocity Model-Harvard (CVM-H, version 15.1.0, *Shaw et al.* [2015], available at `hypocenter.usc.edu/research/cvmh/15.1.0/cvmh-15.1.0.tar.gz`), exemplarily visualized for a cutout in Fig. 2. Velocity and density information are efficiently mapped onto the parallelized computational mesh using the geoinformation server ASAGI [*Rettenberger et al.*, 2016]. The lowest shear-wave velocities v_s (m/s) of the domain and across the fault determine the wave field resolution reached in the simulation. Shear-wave velocities range from 4500 m/s to 320 m/s in the sedimentary basin around the Salton sea. At the fault, shear-wave velocities are 2800 m/s at shallow depths, and do not exceed 3500 m/s at the bottom of the fault, determining the upper bound for subshear rupture speeds. Besides the low-velocity basins at the Salton sea and at the San Bernardino basin (minimum wave speed of 680 m/s) the lowest wave speeds within the high resolution model domain is 900 m/s. The simulation employs viscoelastic rheologies to model intrinsic attenuation [*Uphoff and Bader*, 2016]. We couple Q to the velocity model by using $Q_s = 50.0 v_s$ and $Q_p = 2Q_s$ following commonly used parametrization [*Graves et al.*, 2008]. We discuss the effect of attenuation on dynamically triggered rupture in detail in Sec. 4.4.

Additionally, our model makes use of a computationally efficient implementation of Drucker-Prager off-fault plasticity within SeisSol [*Wollherr et al.*, 2018]. To this end, a domain-wide initialization of initial stresses, cohesion and friction of the bulk (underlying rock) is required, which we base on regional observations from the Landers fault zone area. Here, equivalent initial on- and off-fault stresses are assumed, accounting for the smooth principal stress rotation between the San Bernardino Mountain Domain and the Central Mojave block. Cohesion differs for different rock types, and also depends on depth and the respective damage level of the host rock. In the Landers region, the main near-surface rock type is granodiorite [*Dibblee*, 1967]. Correspondingly, we assume a relatively undamaged granite-type rock, described as "good quality rock" in *Roten et al.* [2017]) who use a Hoek-Brown model to constrain cohesion values for a given rock type and damage level. We therefore define a depth-dependent parametrization of cohesion, ranging from $c = 2.5$ MPa at the surface to $c = 30$ MPa at 6 km depth and $c = 50$ MPa at 14 km depth. While cohesion depends on depth, bulk friction is assumed constant in the entire model domain. We set bulk friction everywhere as equal to 0.55, resembling static friction of most fault segments. While the static friction coefficient of the northern segments is reduced (see previous section), we assume that off-fault rock properties are not considerably altered by paleoseismological events.

In case of plastic yielding, plastic strain at time t can be mapped into the scalar quantity $\eta(t)$ (e.g., visualized in Fig. 10) following *Ma* [2008]:

$$\eta(t) = \int_0^t d\eta = \int_0^t \sqrt{\frac{1}{2}\dot{\epsilon}_{ij}^p \dot{\epsilon}_{ij}^p}. \tag{4}$$

with $\dot{\epsilon_{ij}}^p$ being the inelastic strain rate.

2.5 Numerical Method

We use the open-source software package SeisSol (www.seissol.org; freely available at github.com/SeisSol/SeisSol) to conduct large-scale dynamic rupture simulations of the 1992 Landers earthquake unifying all modeling ingredients described above. SeisSol is based on an Arbitrary high order DERivative-Discontinuous Galerkin (ADER-DG) approach which enables high-order accuracy in space and time [*Käser and Dumbser*, 2006; *Dumbser and Käser*, 2006]. The software solves the non-linear problem of spontaneous frictional failure on prescribed fault surfaces coupled to seismic wave propagation [*De la Puente et al.*, 2009; *Pelties et al.*, 2012]. It allows to precisely model seismic waves traveling over large distances in terms of propagated wavelengths with minimal dispersion errors [*Käser et al.*, 2008] and features fully adaptive, unstructured tetrahedral grids that allow for complicated geometries and for rapid mesh generation [*Wenk et al.*, 2013].

The software is verified in community benchmarks addressing a wide range of dynamic rupture problems including: branched and curved faults, dipping faults, laboratory derived friction laws, and on-fault heterogeneities. [*Pelties et al.*, 2014; *Harris et al.*, 2018]. End-to-end optimization [*Breuer et al.*, 2014; *Heinecke et al.*, 2014; *Breuer et al.*, 2015, 2016; *Rettenberger and Bader*, 2015; *Rettenberger et al.*, 2016] targeting high efficiency on high-performance computing infrastructure includes a ten-fold speedup by an efficient local time-stepping algorithm [*Uphoff et al.*, 2017]. Viscoelastic rheologies are incorporated using an offline code-generator to compute matrix products in a computationally highly efficient way. This poses an increase in computational cost of a factor of only 1.8 in comparison to a purely elastic model (of $\mathcal{O}6$) while resolving the full memory variables [*Uphoff and Bader*, 2016]. Similarly, the off-line code generator is used for incorporating off-fault plasticity within a nodal basis approach [*Wollherr et al.*, 2018]. The computational overhead of off-fault plasticity falls in the range of 4.5% – 13.1% dependent on the number of elements that yield plastically and the polynomial degree of the basis functions. This relatively minor increase of costs enables the use of realistic material properties for large-scale scenarios - and we demonstrate the considerable affects of both, viscoelastic attenuation and off-fault plastic yielding on rupture dynamics and ground motion synthetics in Sec. 4.

The structural model in Universal Transverse Mercator (UTM) coordinates is created with GoCad [*Emerson Paradigm Holding*, 2018] and discretized using the meshing software Simmetrix by Simmodeler [*Simmetrix Inc.*, 2017] to generate a mesh consisting of 20 million elements. For all presented simulations we use a spatio-temporal discretization of polynomial degree p= 4 ($\mathcal{O}5$). The models accounting for off-fault plasticity and attenuation run for 6:53 h on 525 nodes on supermuc phase 1. Note, that the computational costs are higher in comparison to previously presented scenarios [*Wollherr et al.*, 2018] for a similar mesh size due to the additional costs of viscoelastic damping and a higher polynomial degree.

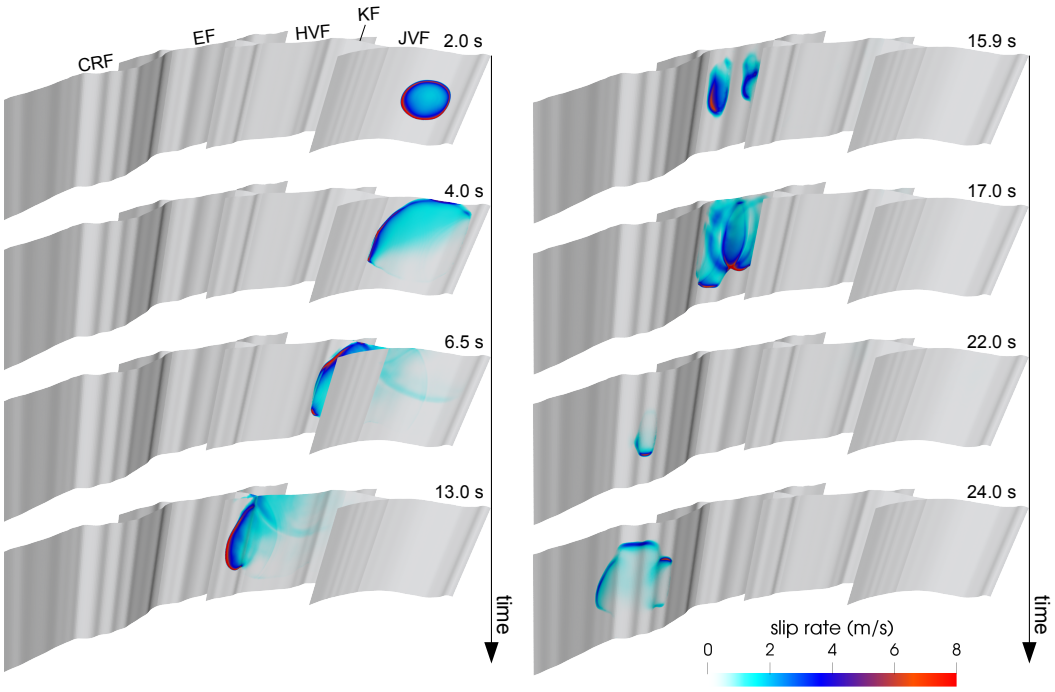

Figure 3. Slip rate across the fault system at selected rupture times illustrating dynamic rupture evolution and complexity. Rupture successively cascades by direct branching and dynamic triggering.

3 Results

In the following, we present a fully 3D dynamic rupture model combining complex fault geometries and off-fault plastic yielding with realistic rheology, viscoelastic attenuation and 3D subsurface structure. Our preferred model reproduces a broad range of regional (moment release, waveforms and peak ground velocities) and near-fault (slip distribution, shallow slip deficit, fault zone damage) observations. The model captures dynamic rupture transfers between fault segments and furthers our understanding of the activation of fault branches and the potential for dynamic triggering of adjacent fault segments.

3.1 Rupture Dynamics

In our dynamic model rupture propagates spontaneously across five fault segments. Rupture successively cascades by direct branching and dynamic triggering. The evolution of slip-rate across the fault segments at selected time steps is visualized in Fig. 3. The fault system overview presented in Fig. 3 is complemented by two additional views focusing on the KF and the branch between the HVF and the EF in the supporting information (Figs. S2 and S3). A high-resolution animation is additionally provided in the supporting information (Movie S1).

Our simulation features very complex rupture propagation patterns. In particular: i) we observe a variety of rupture transfer mechanisms between fault segments:

direct branching, jumping by dynamic triggering, or combination of both, in forward and reverse direction; ii) we find that dynamically triggered rupture transfer is crucial to enable sustained rupture across the entire fault system; iii) multiple rupture fronts exist at certain times that may propagate in opposite directions, and iv) rupture speed is highly variable in correlation with the fault geometry, its orientation with respect to the pre-stress and rupture transfers.

In the following we describe in detail the source dynamics in terms of rupture propagation through the complex fault system. Rupture smoothly nucleates within the first 0.6 s and then spontaneously propagates across the southern part of the Johnson Valley fault segment (JVF). At the fault intersection with the Kickapoo fault (KF), we observe complete rupture transfer by direct branching at high rupture speed at 4 s.

After completely rupturing the KF, slip on the Homestead Valley Fault (HVF) is initiated. However, the pronounced fault bend at the fault intersection nearly stops rupture after approximately 6.5 s rupture time creating localized small slip patches at shallow depths at its northern part. After a delay of almost 1 s, rupture re-initiates at a depth of 7–8 km and continues breaking across the full northern extend of the HVF.

At around 11.9 s, rupture is delayed upon branching into the small fault segment connecting the HVF and the Emerson fault (EF). In distinction to the Kickapoo branching, rupture here also continues along its original branch until it is stopped by the boundary of the HVF segment. The EF is first activated at shallow depth by dynamic triggering from waves originating directly from the HVF which eventually dies out. Rupture is activated for a second time just a few seconds later at depth of 6 km, while a slower propagating rupture front arrives after direct branching via the connecting segment. As a consequence, we observe multiple rupture fronts and reversely (towards the south) propagating rupture, as well as repeated slip of the KF. Parts of the HVF and the KF are dynamically re-activated due to the backward propagating rupture when multiple rupture fronts at the EF meet.

Finally, at 22.3 s rupture time, the CRF is dynamically activated at a depth of 8 km by the superimposed wave field of the subsequent failure of the northern part of the HVF (9 km from the triggered part of the CRF) and the EF (16 km from the triggered part at the CRF). Rupture propagates with a strong up-dip component across the central part of the CRF, and then dies out shortly after reaching the surface. Fault slip completely arrests after 30 s of rupture time.

Our high-resolution model allows to clearly distinguish between rupture branching and rupture (re-)nucleation by dynamic triggering. Rupture chooses to continue along secondary fault segments (branches) whenever these are more favorably orientated than the main fault segment. We observe rupture branching twice: between the JVF, KF and HVF and between the HVF and the EF. In the first case, the optimal orientation of KF towards the background stress field favors rupture propagation. Thus, rupture completely stops at the JVF and rather follows the KF branch. For the second branching transfer (between the HVF and EF), the connecting branch is less favorably oriented. Rupture only partially follows the branch while also continuing along the originating fault segment (HVF).

Dynamic stresses propagate like seismic waves from rupturing fault segments towards locked parts of the fault system, eventually nucleating rupture without requiring the direct arrival of a rupture front. Note that the main rupture front is unable to overcome the geometrical barrier between the EF and the CRF. However, unlike previous dynamic rupture scenarios, our model succeeds in rupturing the CRF by dynamic triggering. This is facilitated by a steep angle of principal stress direction governing the northern fault system, a reduced fault strength, and in particular the emitted seismic waves from the almost simultaneous failure of the northern part of the HVF and

the EF. The stress changes due to failure of both fault segments are high enough to trigger fault slip over a distance of 9 km (from the EF) and 15 km (from the HVF). The abrupt deceleration of rupture in between the KF and HVF additionally triggers small patches of shallow slip at the HVF, but also at the most southern part of the EF, which eventually die out (at around 7.9-9.5s).

Rupture speed v_r is highly variable across the fault system. On average, we find $v_r \approx 2300$ m/s consistent with earlier studies [*Wald and Heaton*, 1994; *Hernandez et al.*, 1999]. Rupture accelerates and decelerates in relation to changes of fault orientation and rupture transfers to adjacent segments. We observe very slow local rupture speeds at geometrical barriers, such as $v_r = 1200\ m/s$ at the transition from the KF to the HVF, and again when rupture reaches the EF.

Supershear transitions are rarely observed in nature, but due to the low resolution of the data it remains still unclear if small supershear patches can occur locally. Small patches of supershear rupture are locally induced in our model at shallow depths. Specifically, we observe supershear due to the interaction of the rupture front with the free surface at the KF and at the HVF, as in previous dynamic rupture models [*Olsen et al.*, 1997; *Peyrat et al.*, 2001]. Additionally, branching triggers local supershear episodes (cf. the JVF-KF branching at approximately 5.6 s rupture time). While localized supershear rupture propagation is not directly enabling rupture transfers, we find that high rupture speeds along the KF facilitate rupture overcoming the fault bend of the HVF.

Rupture termination, and the potential resultant generation of stopping phases, is of specific interest when analyzing rupture in complex, multi-segment fault systems [*Oglesby*, 2008]. From a geological point of view, it was a surprising observation to find that the northern part of the JVF did not slip [e.g. *Rockwell et al.*, 2000]. Our dynamic rupture model provides a consistent explanation for spontaneous rupture termination on most of the principal fault segments, although fault structures in reality continue.

Rupture termination in our model is overall independent of the prescribed geometric fault endings, except for the northernmost section of the HVF where rupture is stopped at the prescribed ending of the fault interface. In all other cases, rupture is spontaneously stopped due to local fault geometry in conjuncture with the local principal stress orientation: First, rupture is smoothly stopped at the first fault segment in backward direction by the change of fault orientation at the most southern part of the JVF. Second, rupture completely follows the Kickapoo branch, not rupturing the northern part of the JVF. Additionally, rupture only initiates in the central part of the CRF and smoothly dies out towards the southern and northern part of the fault. These results are consistent with the rupture termination analysis by *Sieh* [1996] (their Fig. 8).

3.2 Slip Distribution

Numerous studies estimated the on-fault slip distribution of the Landers earthquake [e.g., *Campillo and Archuleta*, 1993; *Wald and Heaton*, 1994; *Cohee and Beroza*, 1994; *Cotton and Campillo*, 1995; *Fialko*, 2004a; *Milliner et al.*, 2015; *Gombert et al.*, 2018]. While theses studies are based on different source inversion approaches and datasets, they overall agree that the largest slip is encountered on the HVF. However, the inferred slip distributions also reveal a large degree of non-uniqueness owing to inherent difficulties in finite-fault slip inversion and the resulting variations in slip models [*Mai et al.*, 2016].

The accumulated slip of our simulation is visualized in Fig. 4. Fault slip is distributed over the southern part of the JVF, the KF, the central and northern part of the HVF, the central EF, and the central part of the CRF. Slip below 1-2 m is

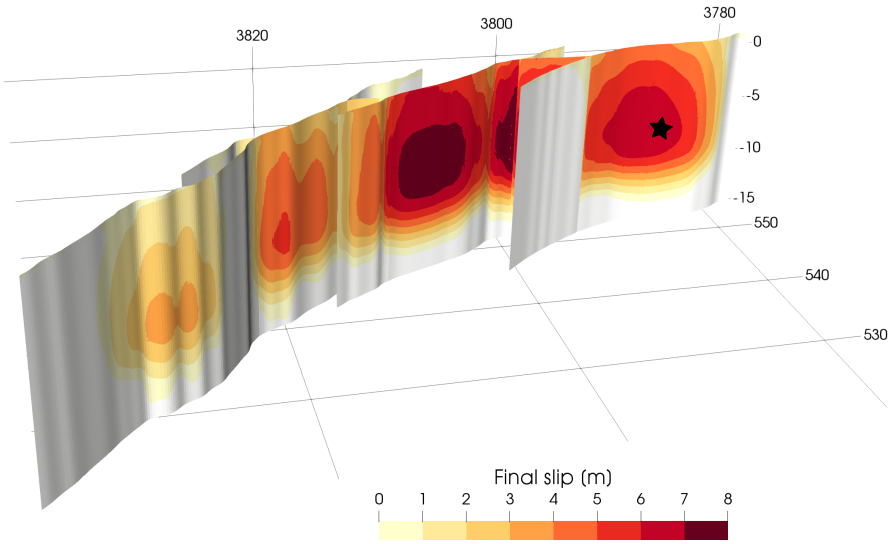

Figure 4. Distribution of total accumulated slip for the preferred dynamic rupture scenario after 100 s simulation time. Coordinate axis are in UTM coordinates (km). The star marks the hypocenter at depth of -7 km.

observed at the southern HVF, and also at the most southern and northern part of the EF where rupture is triggered dynamically. The northern part of the JVF is not ruptured in our simulation.

For all fault segments, slip at depth (5-10 km) is always larger than at shallow depths (less than 5 km). Slip peaks at 7 m located at 5.5 km depth of the central HVF in the vicinity to the KF branching point. At this location, the fault abruptly changes its orientation, forming a geometrical barrier that decelerates the rupture while simultaneously accumulating slip.

In the northern part of the fault system we observe an apparent discrepancy of modeled co-seismic slip with observations. Near-surface slip on the CRF does not exceed 0.5 m in our simulation, while slip at depth reaches up to 4 m. In contrast, the imaged CRF slip values are high at shallow depth [*Sieh et al.*, 1993; *Wald and Heaton*, 1994]. However, *Sieh* [1996] and *Kaneda and Rockwell* [2009] suggest that the CRF might have slipped as a consequence of static stress changes shortly after the main event. We discuss this hypothesis with respect to our simulation results in Sec. 4.5.

3.3 Seismic Moment Rate

The Landers earthquake was the largest earthquake to strike the contiguous United States in 40 years. The event's total seismic moment has been inferred between 6.0e+19–16.0e+19 Nm (moment magnitude M_w 7.15–7.4) [*Kanamori et al.*, 1992; *Campillo and Archuleta*, 1993; *Sieh et al.*, 1993; *Wald and Heaton*, 1994; *Dreger*, 1994; *Cohee and Beroza*, 1994; *Vallée and Douet*, 2016]. The seismic moment of our dynamic rupture scenario equals $M_0 = 11.2\text{e+}19$ Nm (M_w 7.29), in excellent agreement with previous estimates from kinematic models and geological studies.

The multi-segment character of the event reflects on the moment release over time. Most previous studies divide it into two major subevents [*Campillo and Archuleta*,

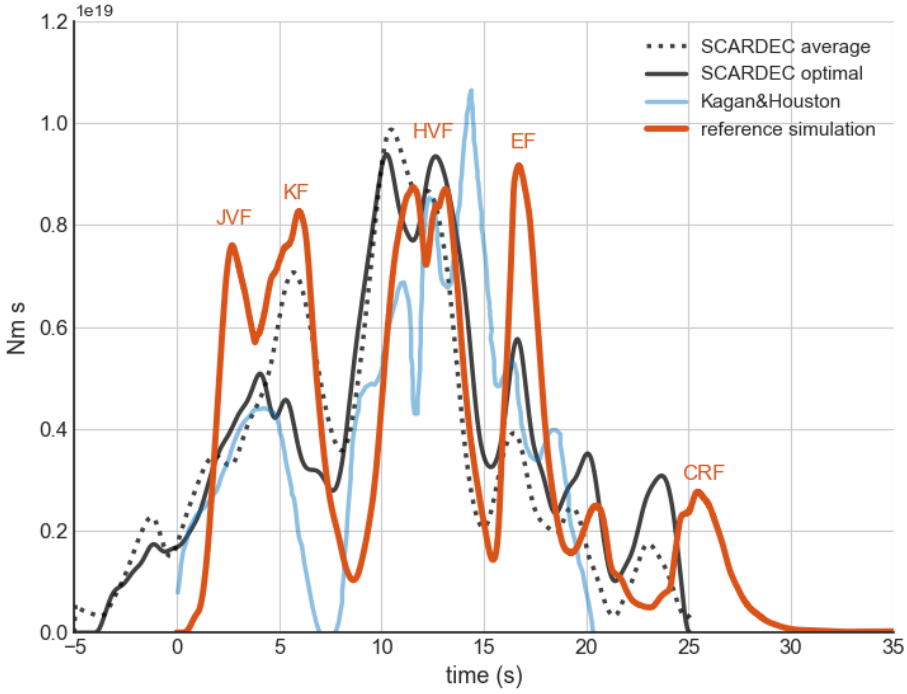

Figure 5. Seismic moment-release rate over time. Dynamic rupture simulation (orange) compared to the optimal and average moment rate of the SCARDEC database (in black and dotted light gray, *Vallée and Douet* [2016]) and moment rate based on the surface slip (in light blue, *Kagan and Houston* [2005]). The time line is taken from our simulation, the SCARDEC solutions are shifted by -5 s accordingly to match the main moment rate peaks as described in the main text.

1993; *Dreger*, 1994; *Cohee and Beroza*, 1994], postulating that slip on the JVF and KF released approximately 20-25% of the total seismic moment, while the northern part of the fault system, including the JVF, the EF and CRF, released approximately 75-80%.

Fig. 5 compares the moment-release rate from our dynamic rupture simulation to three observationally inferred moment-rate functions. The optimal and average seismic moment rate of the SCARDEC database are retrieved from teleseismic body waves (*Vallée and Douet* [2016], gray dotted and black solid lines in Fig. 5). The source time function inferred from the surface slip distribution (*Kagan and Houston* [2005], blue in Fig. 5) is based on the assumption that slip to a depth of 5 km equals to $\approx$ 69% of the surface slip. Note that we use our simulation as reference time, and shift the moment rate release of the SCARDEC solution by 5 s to match the main moment rate peaks. The here required shift in time may be associated with a difference in hypocentral depth between the SCARDEC solution and our dynamic rupture model. While the hypocentral depth determined by the SCARDEC method is 17 km, our dynamic rupture model uses a depth of 7 km, based on inversion results. As a consequence, the SCARDEC inferred moment rate might be delayed in the order of a few seconds [*Vallée and Douet*, 2016].

The seismic moment rate of our simulation reproduces the major moment-rate peaks of the SCARDEC solution well. The first is associated with rupture of the JVF and KF within the first 7 s. The next peak between 7 s and 15 s corresponds to the failure of the HVF releasing the largest individual contribution to overall seismic moment. Subsequently, we reproduce several distinct local peaks after 15 s that we associate with the cascading rupture of the individual northernmost fault segments (e.g. the EF and CRF).

Pronounced delays of moment-release rate in observations as well as our simulation may be correlated with rupture transferring between fault segments. Specifically, dynamic triggering (rupture jumping) has been associated with the observed segmentation of moment release. However, our dynamic rupture model reveals that dynamic triggering is not the only factor reducing the moment release significantly. Specifically, rupture deceleration due to fault geometry strongly affects the moment release, thus complicating the inference of rupture transfers from observations.

Rupture propagation along the HVF (at $\approx$ 7 s) is delayed by $\approx$ 0.5-1.0 s, in the SCARDEC solutions as well as our simulation result. The moment rate provided by *Kagan and Houston* [2005] even accounts for a delay of 2.0-2.5 s and a complete stop of moment release, which may correspond to the observed slip gap near the surface [*Spotila and Sieh*, 1995]. Previous studies interpret this delay of rupture propagation as an indication of rupture jumping from the KF to the HVF[e.g., *Campillo and Archuleta*, 1993]. However, our simulation suggests that this delay rather corresponds to a slow rupture propagation after the branching between the KF and the HVF. Rupture encounters a pronounced fault bend at the center of the HVF and is dynamically slowed down. Rupture re-initiating is then potentially facilitated by arriving seismic waves from the failure of previous segments as discussed in Sec. 4.4.

The most prominent differences in the moment rate functions are found in the early rupture stage. In addition, our scenario overestimates the moment release at 17 s (rupture of the EF) with respect to the SCARDEC solution. However, this high moment rate release at the EF could be related to the highest peak of the moment rate of *Kagan and Houston* [2005] at 14 s. On the other hand, peak moment rates are underestimated around 10 and 15 s (rupture of the HVF and the connecting branch between the HVF and EF). We further discuss these discrepancies in dependence of the model assumptions and artificial nucleation procedure in Sec. 4.1.

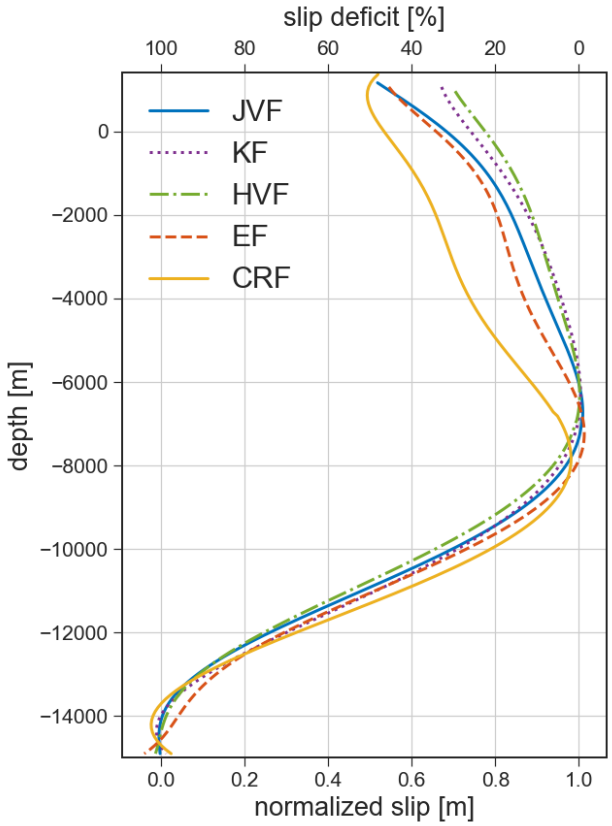

Figure 6. Slip, normalized by each segment's maximum (bottom axis) and corresponding shallow slip deficit (top axis) for each fault segment in dependence of fault depth for the reference Landers simulation. Each line represents the average over the corresponding fault segment.

3.4 The Shallow Slip Deficit and Stress Drop

In this section we investigate the shallow slip deficit (SSD) - the reduction of shallow slip relative to slip at depth - in our simulation. The SSD is frequently observed in geodetic slip inversions for major strike-slip earthquakes, including the 1992 Landers event [e.g., *Fialko*, 2004a; *Milliner et al.*, 2015]. We show that an along-strike variability of the SSD is possible, even for laterally constant rock cohesion and bulk friction.

The SSD of the Landers earthquake is estimated to be of the order of 30-60% [e.g., *Cohee and Beroza*, 1994; *Fialko*, 2004a; *Milliner et al.*, 2015]. Recent coseismic slip models derived by a Bayesian approach suggest that the overall SSD for the Landers event is about 40%, but might vary between fault segments [*Gombert et al.*, 2018].

The origin of the SSD is still under debate. While *Xu et al.* [2016] argue that the majority of inferred SSD is a result of poor resolution of near-fault surface data in slip inversions, it is often attributed to coseismically occurring plastic deformation at shallow depths [e.g., *Kaneko and Fialko*, 2011; *Milliner et al.*, 2015]. Numerical models show that shallow slip is already reduced by 18.6 % in simulations with purely elastic material properties [supplemental material of *Roten et al.*, 2017]. The SSD in their simulations is further increased when accounting for off-fault plasticity, but depends on the underlying bulk cohesion model (higher SSD with lower rock quality).

The modeled SSD on a non-planar yet single fault plane model of the Landers system ranges between 42.9% (good quality rock) and 28.0% (high quality rock) [*Roten et al.*, 2017], consistent with slip inversion results.

Let us compare the resulting slip distribution of our dynamic rupture model (on a segmented fault system and including off-fault plasticity) to inversion results of *Gombert et al.* [2018] and to numerical simulations on a single planar fault plane [*Roten et al.*, 2017]. Recall from Sec. 2.4 that all material properties that influence off-fault plasticity, such as bulk cohesion and bulk friction, are constant along strike.

Fig. 6 shows normalized slip (bottom axis) and corresponding SSD (top axis) of our simulation. The corresponding SSD quantifies the slip reduction within the first 100 m from the surface with respect to the maximum slip, similar to the definition of *Roten et al.* [2017]. We therefore calculate the mean slip across each fault segment within intervals of 100 m depth, considering only slip higher than 0.1 m, and then normalize it by the segment's maximum mean slip. The maximum mean slip is 5.62 m, 6.65 m, 5.46 m, 4.13 m, and 2.34 m for the JVF, KF, HVF and for the CRF, respectively. Note that the SSD functions for different fault segments start at slightly different depths since the fault surfaces intersect with the changing topography.

Our derived SSDs vary between 29.6% and 48.2%, with an average SSD of 40.8%. The highest SSD is found at the JVF (48.2%) and at the CRF (48.0%). An SSD of around 30% is found at the HVF while the KF depict a SSD of 32.9%. Surface slip on the EF is reduced by around 45%. Our results indicate that variations of the SSDs within $\approx$ 20% are possible without any lateral heterogeneity of bulk cohesion. The analysis of the SSD of the corresponding elastic simulation reveals that an even higher variability is present without plasticity (see discussion in Sec. 4.5.) Hence, spatial variations in SSD can be attributed to different fault orientations and the resulting variations in dynamic rupture behavior. While our results agree well with the observational range of 30-60% *Gombert et al.* [2018]'s Bayesian slip-inversion suggests that the maximum SSD of 50% occurred at the HVF, which is underestimated in our model. In contrast, our SSD-values at the JVF and EF are overestimated in comparison to the probabilistic approach of *Gombert et al.* [2018]. Additionally, their shallow slip at CRF is reduced by only 20%, while we observe a SSD of 48.0%.

We infer a relatively high SSD of 50% across the first rupture segments, which may be related to the inferred principal stress orientation. We assume that the hypocentral region is well oriented with respect to the principal stress orientation leading to a large amount of slip at depth. Subsequently, rupture propagates mostly along the Kickapoo branch, preventing larger surface slip at the JVF. The results are independent of the nucleation procedure initiating spontaneous rupture, as discussed in Sec. 4.1.

In Sec. 4.5 we further discuss the implications of our SSD estimates at the CRF segment in the light of recent very low SSD estimates by *Gombert et al.* [2018] and the hypothesis of shallow slip at the northern part of the fault system being triggered statically, shortly after the event, rather than coseismically [*Sieh*, 1996; *Kaneda and Rockwell*, 2009].

We now compare our findings to single fault-plane simulations that include frictional heterogeneity to approximate along-strike variations in fault strength [*Roten et al.*, 2017]. Their reported average SSD of 42.9% is almost identical to the inferred 40.8% using a similar cohesion model but more complex fault structures.

In our model, relatively high stress drops facilitate rupture transfers across geometrical complexities. The scenario features a maximum stress drop of 33 MPa at a depth of 10 km, which is slightly higher than the maximum stress drop of 25 MPa used in Landers-type simulations by *Roten et al.* [2017]. The average stress drop over

all positive slip regions is 12.5 MPa. Such overall high stress drops are consistent with expectations for events with long recurrence time and the inferred global averages from far-field waveforms [*Sieh et al.*, 1993; *Kanamori et al.*, 1992]. However, stress drop estimates contain a large degree of uncertainty: *Sieh et al.* [1993] and *Kanamori et al.* [1992] report for instance 20-28 MPa inferred from the ratio of radiated energy to seismic moment. An analysis of on-fault static stress-drop estimates from kinematic source models for the Landers earthquake, using the method of *Ripperger and Mai* [2004], reveals stress drop averages over all positive slip regions of 6-12 MPa, and maximum stress changes of over 30 MPa within the largest asperities, consistent with our model. However, high stress drops also increase the effect of plasticity, and as a consequence the reduction of shallow slip due to plastic yielding along single fault planes [*Roten et al.*, 2016]. Our model indicates that similar SSD values are possible, even for scenarios with higher stress drop but more complex fault geometries.

Finally, we compute the corresponding radiated seismic energy, using the approach of *Ma and Archuleta* [2006] (their Eq. 5) by subtracting the total frictional work (including fracture energy and heat energy) from the potential energy change due to fault slip. For our reference model, we find a radiated energy of $11.8e+15$ J, which is about 30% higher than the largest value of $8.6e+15$ J reported in *Venkataraman and Kanamori* [2004]. However, *Kanamori et al.* [1992] report a value of $4.3e+15$ J. Obviously, there are large uncertainties (on the order of a factor of 2-3) in published estimates of radiated seismic energy (see also *Kaneko and Shearer* [2015]), likely associated with directivity effects, attenuation models, and data-processing intricacies.

3.5 Ground Motions

In the following, we compare synthetic seismograms of our preferred dynamic rupture scenario to observed waveforms and their peak ground velocities (PGVs). The stations used for comparison are shown in Fig. 7. Site names, Vs_{30}-values the average shear-wave velocity between the surface and 30-meters depth, Joyner-Boore distances R_{JB} (the shortest distance from a site to the surface projection of the rupture surface, and hypocenter-station azimuths are summarized in Table 2. Recorded accelerograms are downloaded from the strong motion data center (`http://www.strongmotioncenter.org/`) and integrated for velocities. Note that the scope of our study is not to fine-tune the model towards detailed waveform fitting. We rather use ground-motion comparisons as an independent, additional source of information after constraining our preferred model to inform us how well (or badly) complex, fully physics-based observations can reproduce observations.

3.5.1 Peak Ground Velocities

The Landers event is a prominent example for a strike-slip earthquake with strong directivity effects, i.e. exhibiting large PGV variability with respect to the azimuth [e.g., *Vyas et al.*, 2016]. Correspondingly, we analyze the PGVs not only in dependence of R_{JB}-distance, but also with respect to azimuth to the hypocenter.

We calculate PGVs using the sensor orientation independent measure GMRotD50 which represents the median of the horizontal motions rotated over all possible rotation angles [*Boore et al.*, 2006]. Fig. 7 is an overview map of our high-resolution model region depicting synthetic PGVs exceeding 5 cm/s. The maximum synthetic PGVs exceed 200 cm/s, and are found in the vicinity of the HVF. We observe a clear directivity effect to the north, north-north-west, while we find strong amplification of ground motions close to the Salton Sea Basin and the San Bernardino Basin due to low S-wave speeds in the subsurface model (see ground motions in Fig. 7).

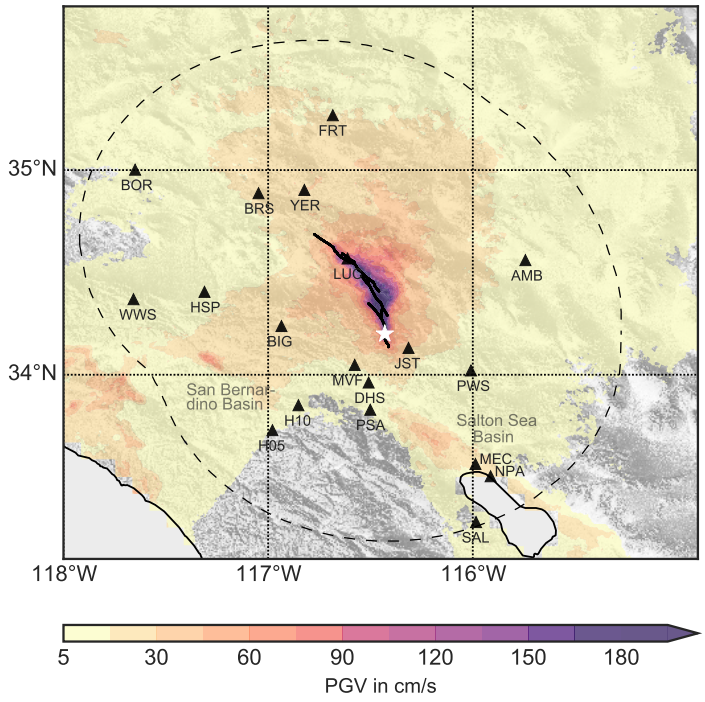

Figure 7. Overview map of the model domain, colored by the simulation's peak ground motions above 5 cm/s based on GMRotD50 [*Boore et al.*, 2006]. The white star marks the epicenter of the 1992 Landers mainshock. Black triangles mark the seismic stations used for comparisons (for details see Table 2). The dashed line denotes the area of R_{JB}-distance of 105 km.

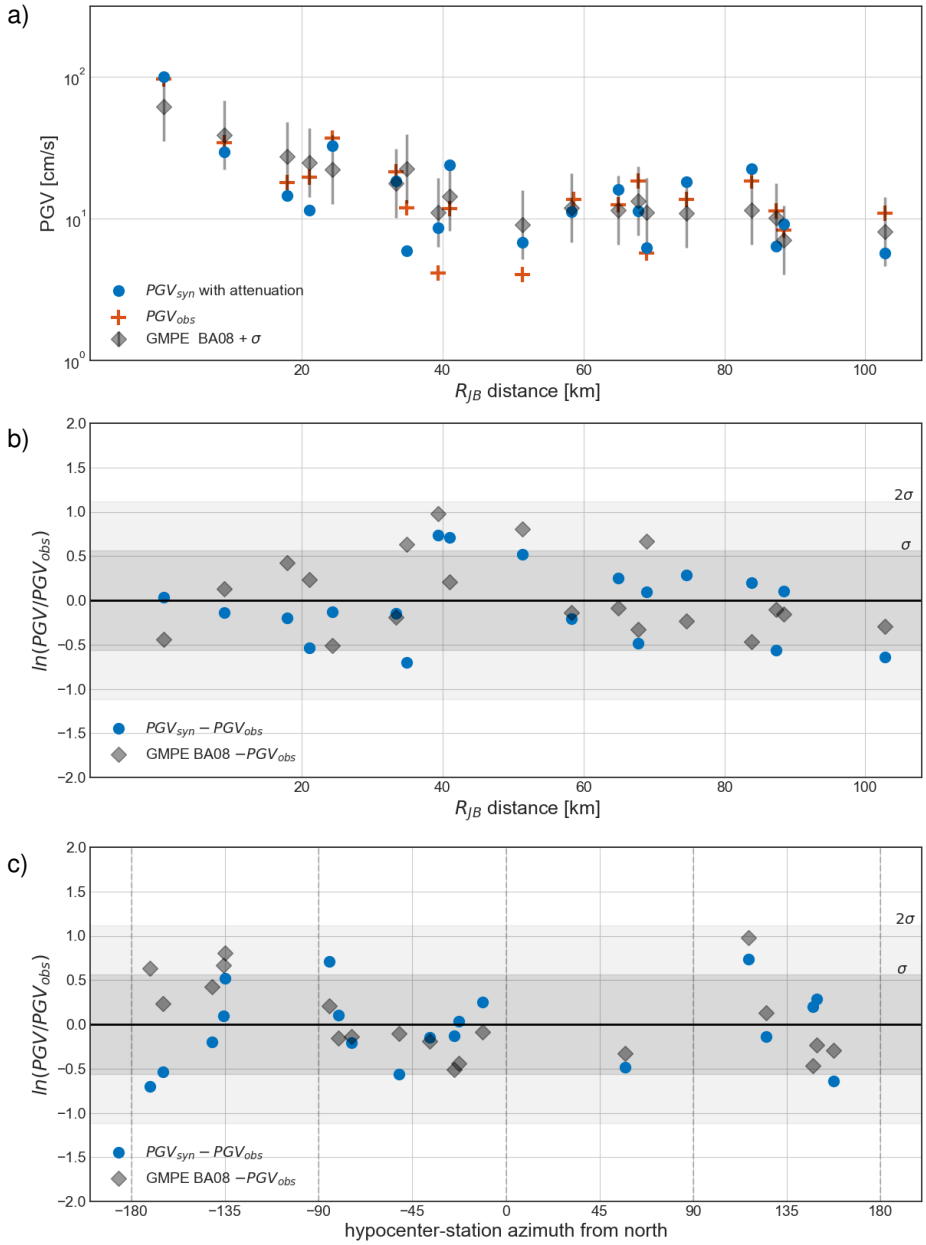

Figure 8. a) PGVs synthetic (PGV_{syn}, blue) and observed (PGV_{obs}, orange) in dependence of Joyner-Boore distance R_{JB} for all stations in Fig. 7. Gray diamonds represent corresponding GMPE values [*Boore and Atkinson*, 2008] (including its standard deviation shown as gray bars). b) PGV-residuals, calculated as $\ln(PGV_{syn}/PGV_{obs})$ for synthetic and observed PGVs (blue dots) and $\ln(GMPE/PGV_{obs})$ for GMPE values and observed PGVs (gray diamonds) in dependence of R_{JB}. c) Corresponding PGV-residuals, in dependence of hypocenter-station azimuth. The dark and light gray shaded areas show the σ and 2σ standard deviation interval, respectively.

station	name	Vs_{30} (m/s)	R_{JB}-distance (km)	azimuth (°)
LUC	Lucern	685.0	0.47	-22.57
JST	Joshua Tree	379.0	9.04	144.77
MVF	Morongo Valley	345.0	17.93	-128.53
DHS	Dessert Hot Springs	345.0	21.12	-105.14
YER	Yermo	354.0	24.37	-25.03
BRS	Barstow	371.0	33.37	-36.77
PSA	Palm Springs Airport	207.0	34.88	-98.76
PWS	Twentynine Palms	685.0	39.37	153.36
BIG	Big Bear	415.0	40.98	-85.0
H10	Silent Valley	685.0	51.32	-134.99
HSP	Hesperia	371.0	58.31	-74.41
FRT	Fort Irwin	345.0	64.97	-11.36
AMB	Amboy	270.0	67.78	57.19
H05	Hemet	339.0	69.0	-134.0
MEC	Mecca	318.0	74.58	120.6
NPA	North Shore Salton Sea	265.0	83.89	122.25
BOR	Boron	291.0	87.33	-51.49
WWS	Wrightwood	506.0	88.41	-80.56
SAL	Salton City	325.0	102.8	112.49

Table 2. Stations used in this study, including site name, Vs_{30}-value (used to calculate the corresponding GMPE values), Joyner-Boore distance R_{JB}, and hypocenter-station azimuth from north. Stations are ordered with respect to R_{JB}-distance.

Fig. 8 a) compares the synthetic (PGV_{syn}) and the observed PGVs (PGV_{obs}) with respect to R_{JB}-distance. We include the standard deviation σ-interval (gray error bars) of the ground-motion prediction equations (GMPEs, gray diamond, *Boore and Atkinson* [2008]) for each station. The corresponding residuals ($\ln(PGV_{syn}/PGV_{obs})$) between the synthetic and observed PGVs, as well as between GMPEs and observed PGVs ($\ln(GMPE/PGV_{obs})$) are depicted in Fig. 8 b).

In general, our simulation results agree very well with the observed PGVs, as all residuals are within two standard deviations. Particular close to the fault, our simulation results agree better with the observations than the values inferred from GMPEs. The largest residuals are found for stations within 39-51 km R_{JB}-distance (stations PWS, BIG, H10, IND) for which the simulations over-predict PGV-values. These four stations are all somewhat in the backward rupture directivity direction, in particular IND and PWS. The back-propagating rupture on the HVF in our scenario may contribute to the locally larger synthetic PGVs.

To analyze a potential azimuthal trend, we plot the residuals with respect to the hypocenter-station azimuth (Fig. 8 c)), defined as the azimuth between the North and the line between the hypocenter and the station. First, we observe an underestimation of the GMPEs with respect to the observations in forward direction ($\approx$ 10-39 °), as also reported by *Vyas et al.* [2016]. In that case, our simulation results reproduce the observations much better than the generic GMPEs do for these stations. Synthetic PGVs in forward direction show very good agreement with the recorded PGVs within one standard deviation. Synthetic PGVs overestimate several stations in backward direction ($>$ 110 °), as mentioned above.

In summary, the peak ground velocities from our simulation results agree well with observations, without any significant error trend with respect to R_{JB}-distance and

hypocenter-station azimuth. The specific effects of off-fault plasticity on the synthetic peak ground motions with respect to the directivity effect is described in the Discussion part (Sec. 4.2).

3.5.2 Waveforms

Next, we examine the seismic waveform characteristics of our simulations, and compare them against observations. Fig. 9 shows three-component seismograms for a selection of stations in forward and backward direction, as well as perpendicular to the fault, ordered by R_{JB}-distance. All seismograms show velocities in cm/s, are bandpass filtered between 0.05 Hz and 1.0 Hz, and are normalized by the maximum value of each component of the recorded seismogram, similar to *Graves and Pitarka* [2010]. The maximum values of each component is annotated above the time series. Some of the observational strong motion recordings lack exact timing information, hence, we cross-correlate them with our synthetics for temporal alignment.

The waveform comparisons show very good agreement between simulations and observations, although not all details of the recordings are reproduced. However, this does not come as a surprise, because our study does not attempt to find an optimized source parameterization to fit waveforms (like in a source inversion study). Still, our synthetic waveforms capture the main S-wave pulses, amplitudes, and shaking duration, indicating the quality of dynamic rupture model.

To quantitatively compare the fit between synthetic and observed waveforms, we use a misfit criteria that evaluates the phase and envelope misfit based on a time-frequency representation of the signals, following the goodness-of-fit measurement (GoF) of *Kristeková et al.* [2009] (their equations 15 and 16). The GoF evaluates the level of agreement and is suitable for comparing observed and synthetic waveforms. The detailed analysis of the waveform misfit can be found in the supporting material, including visualizations of the time-frequency envelope and phase GoFs (Text S2 and Figures S5-S9). The GoF determines a number between 0 (poor) and 10 (identical) to quantify the phase (PG) and amplitude (EG) fit between two signals. The PG and EG for each station and each component are summarized in Table S1 and S2 of the supporting material. In average, we find an EG of 4.70 and a PG of 5.63 which confirms the good agreement between synthetics and observations. The poorest fit is found for the EG of station AMB (2.04), while the maximum Goodness-of-fit values reach close to 8 for the PG of station BOR.

In the forward direction, the main velocity pulses at stations YER and BRS are well reproduced with an average EG of around 5 and average PG of 7. At YER, waveform characteristics and amplitudes agree very well on all three components. For BRS, both horizontal components are very consistent, while for the vertical component the synthetic waveform is substantially larger. For these two stations we also notice that our simulations are not quite able to reproduce the coda-wave behavior following the main pulses, possibly due to the influence of unmodeled small-scale heterogeneity that leads to seismic scattering. This changes, to some extend, for the farther-away stations BOR and FRT. Both are located north of the fault but not exactly in the expected forward-directivity cone. In both cases, the synthetics well reproduce not only the dominant source-related S-wave pulses (of about 5 sec duration), but also the later part of the waveforms (at least in a statistical sense). On all three components, the amplitudes are well matched at stations BOR and FRT as indicated by an EG value in average above 5.

In backward direction (i.e. to the south of the fault system), we obtain good agreement at station DHS for an $\approx$ 10 sec long source-dominated shear-wave that arrives in two distinct wave packages (spaced about 6-7 sec apart). Amplitudes match reasonable well, but coda-waves (due to scattering) are not well reproduced. A similar

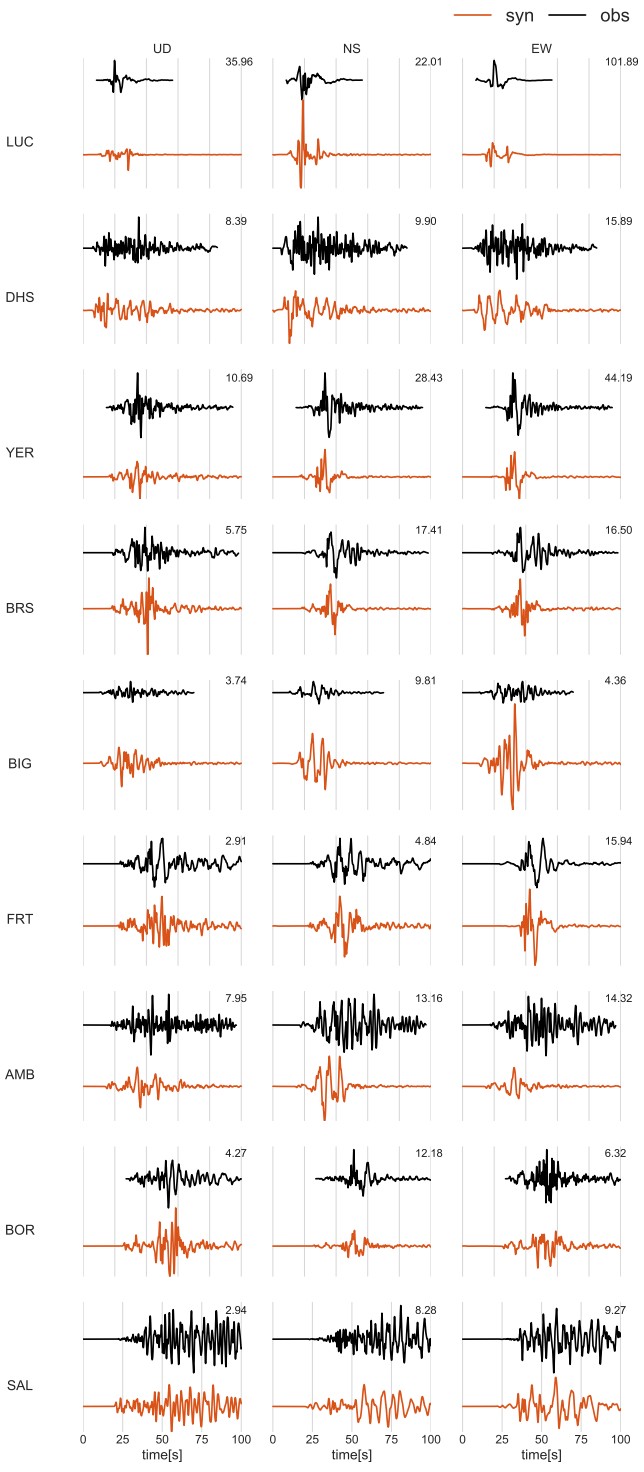

Figure 9. Observed (orange) and synthetic (black) seismic velocities in cm/s for a selection of stations (Fig. 7). All seismograms are bandpass filtered between 0.05 and 1 Hz. The waveforms are normalized by the maximum value of each component of the observation (stated above each trace) and ordered by their R_{JB}-distance.

pattern evolves for stations to the east of the fault (e.g., AMB) and to the west (e.g., BIG). The source-dominated shear-waves are in excellent agreement (though the amplitudes of the synthetics at BIG are higher by a factor 2-5), while the coda behavior is not well reproduced.

We think that for the frequency range considered here, scattering due to topography and a rather smooth 3D Earth model is generally insufficient to generate realistically scattered waves [*Imperatori and Mai*, 2015], thereby affecting the waveform misfit. Note, however, that the farthest recording (at SAL) demonstrates a very consistent overall waveform character, including the coda waves, as regional wave-propagation effects dominate (e.g. the sedimentary basin of the Salton Sea). To reduce the path and side effects and to focus on the source characteristics, we further present the corresponding displacements in the supporting information (Fig. S10).

The closest station to the fault trace, Lucerne station (LUC), recorded strong motions in only 470 m distance from our modeled fault trace of the EF. We note, that the waveform in the synthetic seismogram does not align with observations in terms of amplitudes and phases indicated by low EG and PG, in contrast to the synthetics for other stations in forward direction (such as YER and BRS). Additionally, the amplitude on the north-south (NS) component of LUC is over-predicted by our simulations, while the east-west (EW) component is underpredicted (in each case about a factor 2).

3.6 Off-fault Deformation

During earthquake rupture, the released energy is not only accommodated by frictional sliding on the fault and radiated seismic waves, but is also absorbed by inelastic processes such as plastic deformation in the vicinity of the fault. Off-fault deformation thus poses a key component in the energy budget of earthquakes [e.g., *Rice et al.*, 2005; *Kanamori and Rivera*, 2006]. Relationships between the width of the damage zone and fault displacement provide helpful insight into the associated fault growth and rupture processes [e.g., *Faulkner et al.*, 2011].

Milliner et al. [2015] correlate pairs of aerial photographs before and after the 1992 Landers earthquake to map co-seismic off-fault deformation. The corresponding fault zone width is defined as the perpendicular extend of surface shear to either side of the fault. They find that the magnitude and width of the mapped off-fault deformation correlates with geometrical complexity of fault surface traces.

Fig. 10 compares the accumulated plastic strain distribution at the surface in our simulation with fault zone width (FZW) measurements [*Milliner et al.*, 2015]. Here, we focus on the qualitative characteristics of the synthetic plastic strain distribution and its relation to fault geometry, as the numerical resolution does not allow for quantitatively translating the dynamically induced plastic strain fields into mapped fault damage zones. Our simulation reproduces key features of the mapped fault zone width, in particular the drastic increase of off-fault damage in geometrically complex fault regions. Note, that all simulation results are linked to the here prescribed fault geometry, which cannot account for co-seismic creation of new rupture branches or a new linkage of existing ones.

Following the fault trace from south to north, an increase of FZW for both the mapped and modeled damage zones can be observed, particularly at the southernmost part of the JVF. Close to the branching point to the KF, at around 3795 km UTM Northing and 550 km UTM Easting, our model predicts an increase in plastic deformation on the extensional side of the fault which agrees with the FZW of *Milliner et al.* [2015]. The region with highest plastic strain between 3800-3810 km UTM Northing is clearly correlated with the observed increase of the FZW. Although the southern-

most part of the EF did not fully rupture in the simulation, shallow fault slip still triggers plastic deformation very narrowly around the fault trace. Both models show an increase in fault zone complexity at the transition of the HVF and EF (see inset to Fig. 10). In particular, the dynamic rupture scenario reveals how the accumulated plastic strain connects the ends of the HVF and the EF. The northernmost part of the fault system lacks off-fault plastic deformation, owing to the lack of shallow slip at the CRF.

Due to the lack of observational constraints, the our models include laterally homogeneous plasticity parameters (bulk cohesion and bulk friction). While the major features of the modeled off-fault deformation pattern are related to the changing fault orientation, the existing discrepancies might be related to missing heterogeneous structure along the fault segments. Off-fault deformation correlates with the near-surface lithology that either promote or prevent off-fault damage [*Zinke et al.*; *Milliner et al.*, 2016].

An observed increase of the FZW close to the hypocenter suggests that the fault zone structure may be locally more complex than our modeled fault-surface representation. Accounting for a more complex geometry would potentially slow down rupture and/or reduce the energy release at the JVF [*Zielke et al.*, 2017] (see also Sec. 4.1). Small-scale fault roughness, as observed for natural faults [e.g., *Candela et al.*, 2012], is not included in our model, but potentially may lead to a strong signature in the simulated plastic deformation [*Dunham et al.*, 2011a; *Shi and Day*, 2013].

At the transition between the HVF and EF, our model accounts only for one branch, while fault trace mapping shows two subsequent branches to the EF [*Sieh et al.*, 1993; *Milliner et al.*, 2015]. The increase of plastic strain at the HVF results in a rapid decrease of rupture speed in the vicinity of its geometrical barrier (fault bend). Interestingly, this plastic strain exactly connects the HVF and EF where the second branch is observed. Hence, this connection may have been created or enhanced during the 1992 Landers event. In order to investigate whether a connecting branch slipped co-seismically, future simulations would need to explicitly include such segment into the prescribed fault network geometry.

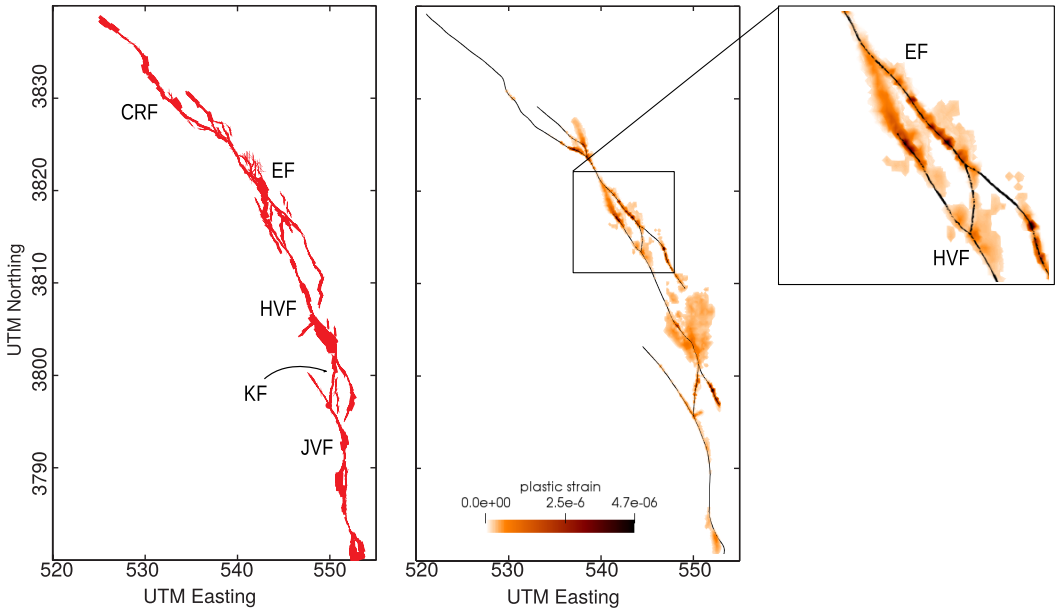

Figure 10. Fault zone width (FZW) compiled by *Milliner et al.* [2015] from aerial photograph correlations (left) in comparison to the accumulated plastic strain from the presented dynamic rupture simulation (middle). The right figure shows an inset at the transition from the HVF to EF.

model name	visco-elasticity	plasticity	stress along the KF	critical slip distance D_c
reference simulation VP-KF0-062	yes	yes	KF0	0.62 m
VP-KF1-062	yes	yes	**KF1**	0.62 m
VP-KF2-062	yes	yes	**KF2**	0.62 m
VE-KF0-062	**no**	yes	KF0	0.62 m
VE-KF0-072	**no**	yes	KF0	**0.72 m**
P-KF0-062	yes	**no**	KF0	0.62 m

Table 3. Summary of the model variations discussed in Sec. 4 and their abbreviated names. The details of the varying rotation of stresses governing the Kickapoo fault in models VP-KF0/KF2-062 are explained in Sec. 4.1. The elastic models VE-KF0-062 and VE-KF0-072 are compared to the reference model in Sec. 4.2, while the influence of attenuation (comparison between the reference model and model P-KF0-062) is discussed in Sec. 4.4.

4 Discussion

Sustained rupture along the geometrical complex fault of the 1992 Landers earthquake provides strong constraints on the model parametrization such as stress orientation, stress amplitudes and friction. Our source model shows excellent agreement with estimated moment-release rate, recorded PGV's, and key features of the observed off-fault deformation patterns. We discuss in the following further implications, potential improvements, but also the sensitivity to variations in prior assumptions of the preferred dynamic rupture model (hereafter named the reference simulation). The variations of the discussed models and their abbreviated names are summarized in Table 3.

4.1 Early moment release and earthquake initiation

The presented Landers earthquake scenario slightly overestimates moment release within the first 10 s (Fig. 5) compared to the SCARDEC solutions [*Vallée and Douet*, 2016]. The higher moment release occurs during nucleation, rupture across the JVF and branching into the KF. It has been shown that rupture initiation of spontaneous rupture simulations is highly sensitive to the choice of numerical nucleation procedure [*Galis et al.*, 2014] and initial stress and strength on- and off-fault [*Gabriel et al.*, 2012, 2013] in the hypocentral region. We here discuss potential reasons and improvements specifically with respect to earthquake nucleation and the parametrization of the first segments of the fault system.

Dynamic rupture simulations are initiated by an artificial nucleation procedure on a pre-defined nucleation patch (see Sec. 2.3). In our simulation, this leads to a rapid start of rupture, which is further enhanced by the favorable orientation of the hypocentral fault region with respect to the regional stress field. However, observations indicate that rupture started gradually during the first 3 seconds, likely due to a small foreshock in the vicinity of the epicenter [e.g., *Campillo and Archuleta*, 1993; *Abercrombie and Mori*, 1994].

In our modeling, we find that rupture dynamics and associated moment release remain robust across the first fault segment when varying nucleation patch size, forced rupture time or forced rupture speed within the nucleation patch. This allows to also examine if the prescribed nucleation procedure affects spontaneous rupture behavior

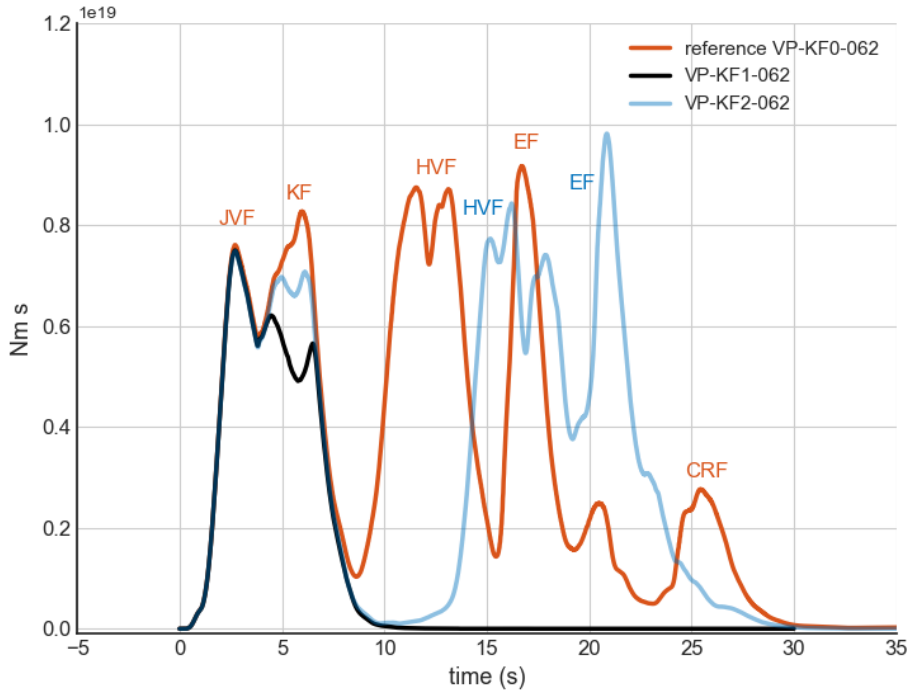

Figure 11. Seismic moment-release rate of the reference simulation (orange) in comparison to two models with changed principal stress orientation governing the KF: Model VP-KF1-062 (black) assumes a linear transition of the stress regime of the JVF to the HVF (33° to 20°) starting at the beginning of the KF and ending at the intersection with the HVF. Model VP-KF2-062 (light blue) features the same transition to 20° at the HVF but starting in the center of the KF.

at the JVF. Spontaneous rupture is delayed, but still initiates for radii as small as 0.5 km. For larger radii (up to 4.5 km), rupture initiates faster, however, the moment-release rate remains unchanged. Similar behavior is found for varying the time of the forced nucleation t_{nuc}: for shorter nucleation times (0.2 s) rupture initiates faster, but spontaneous rupture outside the nucleation patch is identical. We find that rupture speed and moment-release rate outside the nucleation patch are not changed by varying the forced rupture speed within the nucleation patch v_{nuc} in the range of 2000 m/s to 3300 m/s.

Mapped surface traces and off-fault deformation distributions indicate that structural complexity is enhanced close to the hypocenter [*Liu et al.*, 2003; *Milliner et al.*, 2015]. The rapid rupture initiation could potentially be delayed by considering fault structures more complex than the curved, yet purely strike-slip fault geometry used in our simulation. Including small-scale geometrical roughness may additionally slow down rupture and limit the stress drop [*Dunham et al.*, 2011b; *Shi and Day*, 2013; *Zielke et al.*, 2017; *Mai et al.*, 2017], while simultaneously increasing off-fault damage.

The 5 km short connecting Kickapoo fault (KF) plays a crucial role for early moment release by linking the Johnson Valley (JVF) and Homestead Valley (HVF) faults. Despite its short length, it slipped with a maximum of nearly 3 meters, and may have hosted the initiation of the March 15, 1979, Homestead Valley earthquake

[*Hill et al.*, 1980; *Sowers et al.*, 1994]. However, local principal stress orientation are not well constrained, since it is debated whether this fault branch is part of the San Bernardino or the Central Mojave domain.

We observe a second relatively high peak of moment-release rate at around 6 s (see Fig. 11) related to slip at the KF. Decreasing the angle of principal stress orientation acting on this fault step-over branch reduces this peak. In our reference model (Sec. 2.2), the KF experiences an equivalent angle of maximum compressive stress (33°) as the JVF (hereafter referred to as KF0). However, if the KF already constitutes the transition between the San Bernardino and the Central Mojave domains, its local stress orientation might be steeper.

Therefore, we test two variations in stress orientations across the KF, which respectively vary its strength while rupture in all three models is initiated by the same nucleation procedure. First, background stresses smoothly rotate from 33°, starting at the beginning of the KF and reaching 20° at the intersection with the HVF (model VP-KF1-062 with rotation KF1). The black line in Fig. 11 demonstrates the reduced moment-release rate between 4-7 s, related to rupture on the KF, for this case. However, subsequently rupture is coming to a complete halt at the JVF, and thus is unable to propagate across the remaining fault segments.

Second, we test the hypothesis that the initial part of the KF is favorably oriented (33°, to promote branching), while stresses start to rotate to 20° only in the center of the KF (model VP-KF2-062 with rotation KF2, light blue line in Fig. 11). In this case, the moment-release rate between 4-7 s is still decreased with respect to the reference model, but not as pronounced as for model variation 1. Rupture initiation at the HVF is drastically delayed - by 5.5 s in comparison to the reference model. After re-initiation, rupture overcomes the fault-bend barrier and breaks the entire fault system. The rupture path is very similar to the reference model, highlighting the robustness of the source dynamics described in Sec. 3.1.

Our numerical experiments therefore suggest a locally steeper angle of principal stress orientation in order to better match the estimated moment-release rate within the first 10 s of rupture. However, such principal stress orientation may require other mechanisms facilitating rupture transfers, such as: i) more complex fault geometries, including additional connecting fault segments as seen in fault traces by *Liu et al.* [2003], ii) fault weakening mechanisms, such as strong velocity-weakening friction or the effect of thermal pressurization, since there is evidence of a fluid-saturated upper crust, [*Fialko*, 2004b], iii) compliant fault zones with reduced rigidity promoting rupture propagation [*Finzi and Langer*, 2012a]. Investigating the effects of these physical mechanisms on the dynamic rupture process of the Landers earthquake will be hopefully addressed in future work, but is beyond the scope of this study.

4.2 The Effect of Off-fault Plasticity on the SSD, Rupture Transfer and Moment Rate

In nature, high stresses during earthquake rupture are accommodated by inelastic processes near the crack tip, but also in the bulk, such as plastic deformation of the host rock. Off-fault plastic response is an important physical process that needs to be considered in realistic models of rupture dynamics, for example to limit on-fault stresses and slip rates as well as peak ground shaking levels [*Andrews*, 2005; *Roten et al.*, 2017] and to enable comparisons with mapped off-fault deformation patterns [*Milliner et al.*, 2015]. Plastic strain accumulates when the rupture path deviates from planarity, e.g., at changes of fault strike orientation, branching, or segment endings. *Wollherr et al.* [2018] demonstrate the influence of non-elastic material behavior on the spatio-temporal rupture transfer processes across the geometrical complexities of the Landers fault system. Off-fault plasticity also delays rupture arrivals across the entire fault,

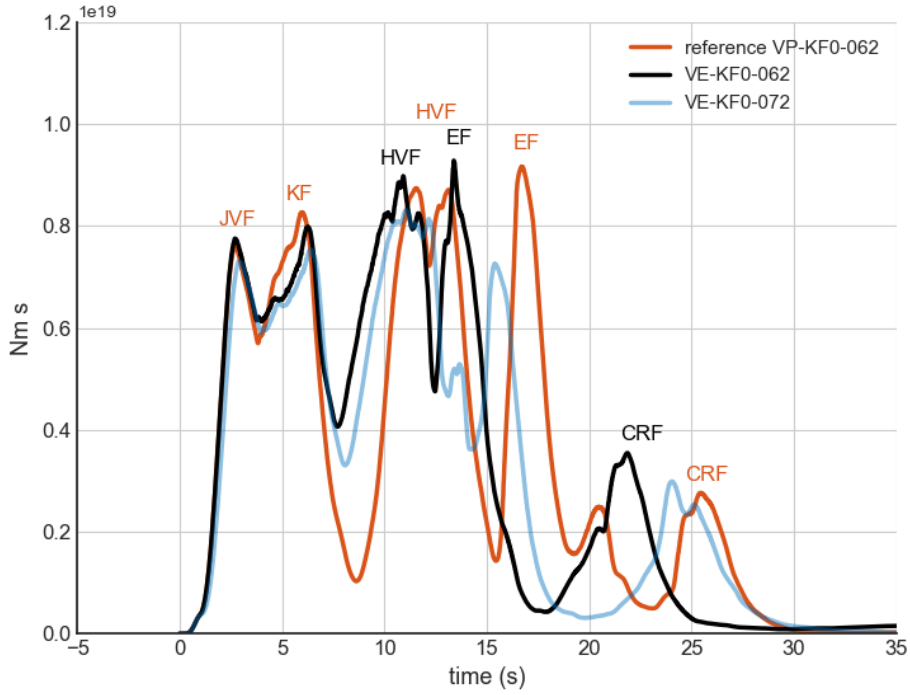

Figure 12. Seismic moment-release rate of the reference simulation including off-fault plasticity (VP-KF0-062, orange), compared to an identically parametrized but purely elastic simulation (VE-KF0-062, black), and an elastic simulation with a higher critical slip distance D_c (VE-KF0-072, light blue).

even to a larger extend than reported for scenarios on planar faults [*Roten et al.*, 2015; *Wollherr et al.*, 2018]. In direct comparison of purely elastic scenarios and those including plasticity, slip is found to be locally higher but more concentrated. As a result, moment magnitudes are comparable with and without plasticity, even though the rupture path differs dynamically.

We now compare the results of our reference model that includes off-fault plasticity to simulations with purely elastic material properties (model VE-KT0-062), and discuss the effect of off-fault deformation on the corresponding SSD, moment-release rate and rupture transfer on this complex-fault system. The normalized slip and the corresponding SSD of the purely elastic simulation is visualized in the supporting material (Fig. S4, similar to Fig. 6). The inferred SSD falls in between 11.7% and 44.2%. The highest SSD is found at the JVF (44.2%). An SSD of 32.2% and 35.8% is found at the KF and the EF, respectively. Slip in the shallow part is reduced by 20.5% at the HVF and by 11.7% at the CRF.

In contrast to the reference simulation with plasticity, the purely elastic simulation depicts lower SSDs along all fault segments. The SSD is increased between 0.7% (KF) and 36% (CRF) by plasticity. Interestingly, along-strike spatial variations of the SSD of up to 33% become apparent also in the elastic simulation (with plasticity: 20%). As a consequence, the spatial variations can be attributed to the fault geometry and velocity structure and their influence on the resulting rupture dynamics, rather than to the influence of the heterogeneous occurrence of off-fault plasticity.

While the estimated SSDs of the Bayesian approach of *Gombert et al.* [2018] along some segments show better agreement with the reference simulation including plasticity (i.e. at the HVF), their SSDs along other segments is better represented by the purely elastic results (i.e. at the CRF). In addition to the influence of the fault geometry and the resulting rupture dynamics on the spatial variation of the SSD, these results suggest that off-fault deformation might be more pronounced on some segments than on others. However, our reference model accounting for off-fault plastic deformation is characterized by laterally homogeneous plasticity characteristics (cohesion and friction of the host rock). Further information of lateral varying plastic material properties such as bulk cohesion and bulk friction that control the amount of plasticity along each fault segment might therefore be taken into account in future simulations.

Fig. 12 depicts the corresponding moment-release rate of our reference simulation (model VP-KT0-062, orange) to an equivalent scenario assuming purely elastic material response (model VE-KT0-062, black). The model parameterization is otherwise exactly the same. The resulting seismic moment is $M_0^{ela} = 11.102\text{e+}19$ Nm (M_w^{ela} 7.292), compared to $M_0 = 11.106\text{e+}19$ Nm (M_w 7.293) of the reference simulation with off-fault plasticity.

While the overall seismic moment is almost identical for both cases, the moment release is distributed slightly differently during the intermediate rupture stage: We find that rupture transfers across geometrical barriers are generally enhanced if off-fault plasticity is neglected. The rupture transfer between the KF and the HVF is facilitated by the purely elastic material response (at 11 s in Fig. 12), and rupture also transfers faster between the HVF and EF, leading to a smaller gap in moment rate release (at 12 s). Consequently, rupture at the CRF is initiated $\approx$ 5 s earlier than in the simulation with off-fault plasticity (compare the last moment rate peak for both scenarios).

The comparison of the reference model to the corresponding purely elastic model (VE-KF0-062) suggests that off-fault plastic deformation may vary along-strike and specifically may be less pronounced across the CRF, similar to our findings with respect

to the SSD. Future models may explore the interaction of rupture transfers, plastic deformation and spatially varying bulk cohesion and friction models in dependence of each fault-segment or even smaller scales.

Interestingly, our numerical tests reveal that fully elastic simulations can partially emulate the reference simulation when increasing the critical slip distance D_c. In this case, moment-release rate and rupture transfer dynamics are preserved, but exhibit slower rupture speeds and longer delays when transferring to adjacent segments due to an increased critical size [e.g., *Ampuero et al.*, 2002; *Bizzarri*, 2010; *Galis et al.*, 2014] to initiate self-sustained rupture by dynamic triggering.

For simulations based on linear slip weakening friction including off-fault plasticity (i.e. the reference case), we find that both, relatively high stress drops and a relatively low critical slip distance of $D_c = 0.62$ m, are required to sustain rupture along the segmented faults. In particular, the geometrical barrier at the center of the HVF, as well as the transition between the HVF and the EF, pose strong boundary conditions for sustained rupture. When increasing only as much as to $D_c = 0.64$ m we observe rupture delays of more than 5 s between the KF and the HVF. For values of $D_c > 0.64$ m we observe a complete stop of rupture before breaking all segments.

In the corresponding elastic simulations, rupture transfers are facilitated by the lack of plastic deformation in the vicinity of geometrical barriers [e.g., *Wollherr et al.*, 2018]. For example, by increasing D_c to 0.72 m in the elastic simulation (i.e. increasing the fracture energy by 16%), rupture and the transition between distinct fault segments are distinctly slowed down (model VE-KT0-072, light blue line in Fig. 12). However, the resulting seismic moment of $M_0^{ela} = 10.057\text{e+}19$ Nm (M_w^{ela} 7.279) is very similar to the seismic moment of the reference simulation.

4.3 The Effect of Off-fault Plasticity on Peak Ground Motions

Let us examine the effects on peak ground motions for these three scenarios. Ground motions in seismic hazard assessment are typically described by Ground Motion Prediction Equations (GMPEs) that depend mainly on event magnitude, source-to-site distance, and site-effects (e.g. the Vs_{30}-value), but other source-related and path-related effects may be important, too. However, standard GMPEs fail to describe ground motions of earthquakes with strong directivity effects, varying rupture speed or 3D velocity structures including low-velocity basins [e.g., *Graves et al.*, 2008; *Spudich and Chiou*, 2008; *Ramirez-Guzman et al.*, 2015]. Therefore, dynamic rupture simulations like ours are useful to possibly complement GMPEs by exploring physically possible parameter spaces.

Ground motions in dynamic rupture simulations on single faults are reduced by off-fault plastic yielding [*Roten et al.*, 2014, 2015], however, the combined effects of plastic deformation, physics-based dynamic rupture transfers, and directivity on the ground motion properties for complex-geometry faults has not yet been analyzed. For this purpose, we examine the mean peak ground motions and their variability for the three scenarios discussed above. The corresponding PGV maps can be found in Appendix C: .

4.3.1 Azimuthal Dependence of PGVs

First, we analyze the dependence of peak ground velocities (PGVs) on receiver-epicenter azimuth to help understand directivity effects in our simulations under different material responses. Interestingly, this effect has not yet been analyzed systematically for dynamic rupture simulations with and without off-plasticity. Our results show that off-fault plasticity reduces the mean PGVs mainly in forward direction, while

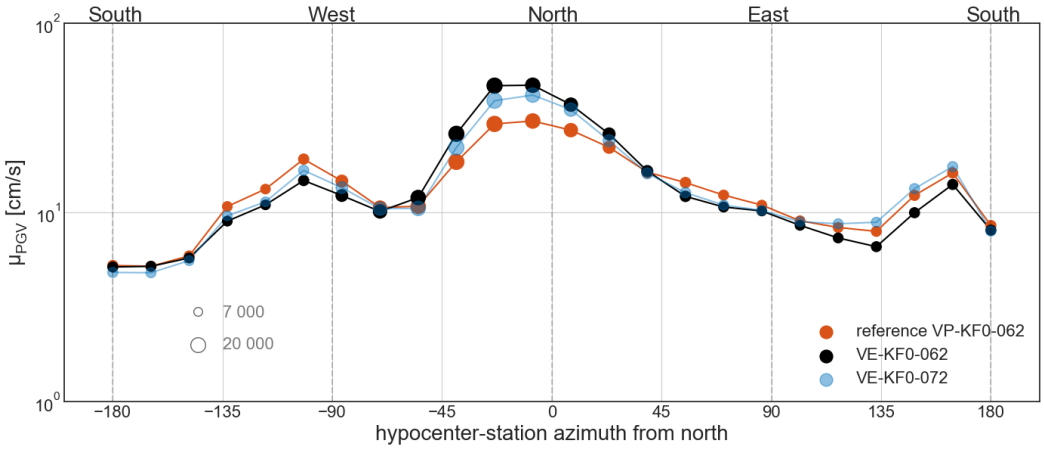

Figure 13. Azimuthal dependence of a) mean PGV denoted as μ_{PGV} for the reference simulation (orange), the corresponding elastic simulation (black) and the elastic simulation with increased D_c (light blue) for all stations between 1 km and 105 km R_{JB}-distance (bin width = 20 km). The circle radii represent the number of stations in each bin.

they are increased in backward direction. This effect can be only partially mitigated by decreasing the rupture speed (e.g., by increasing D_c) in purely elastic simulations.

We calculate the PGVs of 250 000 synthetic stations distributed within 1 km and 105 km R_{JB}-distance of the fault trace using GMRotD50 [*Boore et al.*, 2006]. These stations are binned with respect to their azimuth to the epicenter with a bin width of 15°, resulting in at least 7000 stations per bin.

Fig. 13 shows the azimuthal dependence of the mean value of PGVs μ_{PGV} calculated for each bin and for all three scenarios. We observe differences in absolute PGVs between our scenarios, especially in the forward and backward directions. The purely elastic simulation model VE-KT0-062 (black) exhibits the highest μ_{PGV} reaching up to 47.1 cm/s in forward direction (between -30° and -15°). The increase of D_c from 0.62 m to 0.72 m (model VE-KT0-072) decreases μ_{PGV} by up to 11% in forward direction. Plasticity reduces μ_{PGV} by up to 35% compared to an identical elastic simulation with $D_c = 0.62$ m. However, the directions between -90° and -45° and 45° and -135° experience very similar μ_{PGV} for all three scenarios. In backward direction (between 150° and 165°), μ_{PGV} is elevated and peaks for the simulation with off-fault plasticity and the elastic simulation with increased D_c.

While some of the increase of μ_{PGV} in backward directivity is attributed to the low velocity basin around the Salton Sea that generates basin-amplification effects (see Fig. 7), we can also attribute our results to the geometrical complexity of the fault system. Rupture propagation is slowed down at geometrical barriers or fault branches by the occurrence of plastic yielding which leads to an increase of reversely propagating rupture. We observe that lower rupture speeds and longer delays at geometrical barriers lead to more backward traveling seismic waves which further increase PGVs in backward direction.

We conclude that the effect of plasticity can only be partially emulated by a rupture speed decrease (e.g. increasing D_c) in purely elastic simulations: the simulation with plasticity and the elastic simulation with increased D_c show similar μ_{PGV} between -180° and -45° and 45° and 180°, but the purely elastic simulation still overestimates the directivity effect between -45° and 45°.

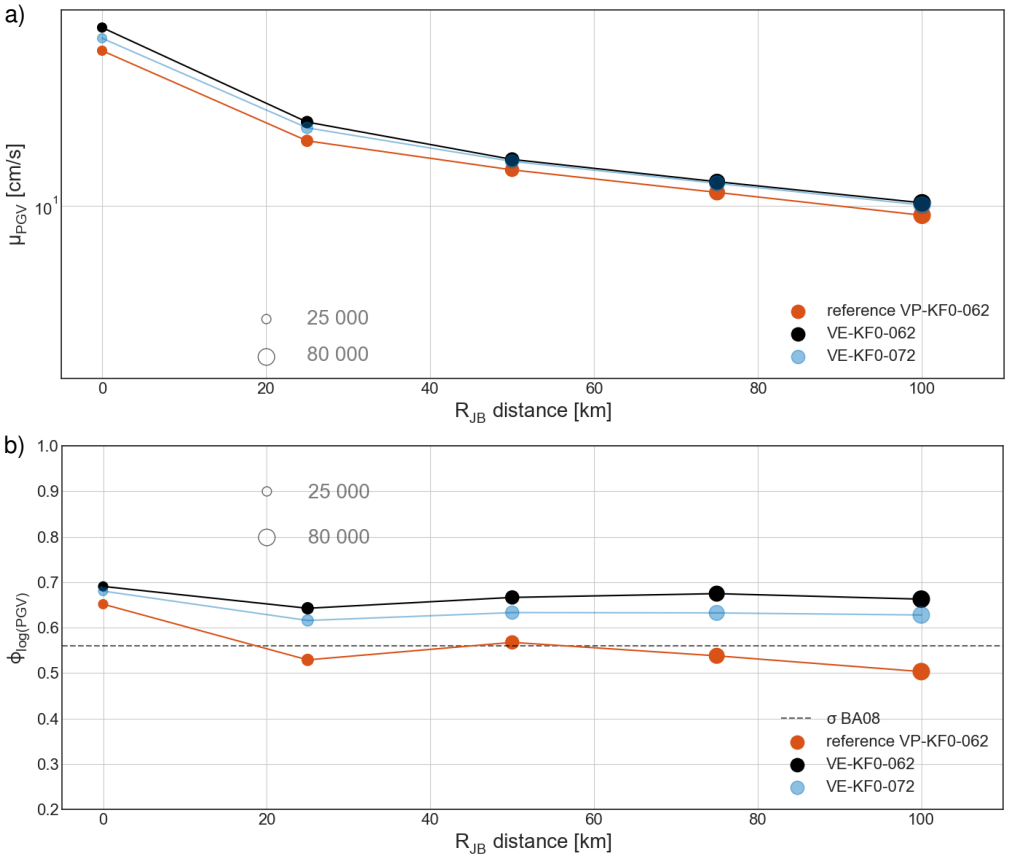

Figure 14. Distance dependence of a) the mean PGV μ_{PGV} and b) standard deviation $\phi_{\log(\mathrm{PGV})}$ for the reference simulation with plasticity (orange), the corresponding elastic simulation (model VE-KT0-062, black) and the elastic simulation with increased D_c (model VE-KT0-072, light blue) for all stations between 1 km and 105 km R_{JB}-distance (bin width = 20 km). The circle size represents the number of stations in each bin. The dashed line in b) represents the constant standard deviation of the GMPE of *Boore and Atkinson* [2008].

4.3.2 Distance Dependence of PGVs

Let us now investigate the distance dependence of the mean PGVs μ_{PGV} for the three simulations. Plastic yielding primarily appears in the vicinity of the fault, but corresponding PGV maps show PGV reductions (beyond the standard geometrical spreading) over large distances [*Roten et al.*, 2014]. To investigate this effect systematically, all stations are binned with respect to their R_{JB}-distances using a bin widths of 20 km (at least 25 000 stations per bin). Fig. 14 a) shows the mean PGV μ_{PGV} for each of these bins.

In general, the elastic simulations show higher μ_{PGV} over all distances in comparison to the reference simulation with plasticity. Larger differences are visible close to the fault where plasticity reduces μ_{PGV} by 21.9% within the first 20 km, while μ_{PGV} is reduced by on average 12.4% between 85 km and 105 km R_{JB}-distance. By increasing D_c in the purely elastic simulations, μ_{PGV} is reduced by 10.8% within the first 50 km (still 12.4% difference to the simulation with plasticity), but shows almost identical behavior for larger distances compared to the elastic simulation with $D_c = 0.62$ m.

GMPEs commonly assume a constant ground motion variability [*Boore and Atkinson*, 2008], independent of the distance to the fault. However, a distance dependent variability is found for kinematic simulations of the Landers earthquake assuming purely elastic material properties [*Vyas et al.*, 2016]. Different ground motion variability values might have a significant impact on the results of seismic hazard analysis [e.g., *Restrepo-Velez and Bommer*, 2003; *Bommer and Abrahamson*, 2006; *Strasser et al.*, 2009]. Here, we additionally investigate the distance dependence of ground motion variability in dynamic rupture simulations on complex faults including off-fault plasticity.

Fig. 14 b) shows the standard deviation of the logarithmic PGVs $\phi_{\log(\mathrm{PGV})}$ for each bin in comparison to the constant value of 0.56 used by the GMPE of *Boore and Atkinson* [2008]. The variability is in general higher than 0.56 for the purely elastic simulations although $\phi_{\log(\mathrm{PGV})}$ is already reduced by 4.4% in average when we increase D_c. The simulation with plasticity shows the smallest ground motion variability, ranging from 0.65 (0-20 km bin) to 0.50 (85-105 km bin), very close to what is used in GMPEs by *Boore and Atkinson* [2008]. In the simulation with plasticity, high stresses are limited by plastic yielding, which results in a reduction and smoothing of on-fault slip rates [e.g., *Wollherr et al.*, 2018]. As a consequence of the smoother peak slip rates, the resulting ground motions have lower variability.

Overall, we observe only a small distance dependence of ground motion variability for the simulations using purely elastic rock properties, in contrast to what is reported by *Vyas et al.* [2016]. However, they employ kinematic source models of the 1992 Landers earthquakes using a second order accurate generalized finite-difference code [*Ely et al.*, 2008]. They find that the variability is much higher close to the fault (in average 0.79), and reduces to a constant value of 0.6 only at 100 km distance (Fig. 5 in *Vyas et al.* [2016]).

We argue that the smoother final slip distribution of our dynamic rupture source models is responsible for the lower variability of simulated ground motions. In our model, the highest slip is always located at depth, and it is very smoothly distributed across the fault segments (Fig. 4). In contrast, *Vyas et al.* [2016] use kinematic source models of *Cotton and Campillo* [1995]; *Hernandez et al.* [1999]; *Zeng and Anderson* [2000]; *Wald and Heaton* [1994] and *Cohee and Beroza* [1994] which all feature very heterogeneous slip distributions, that is, slip occurs in isolated patches. Also, four out of their five models contain zones of large near-surface slip that may lead to an increased variability of ground motions in the vicinity of the fault. *Vyas et al.* [2016]

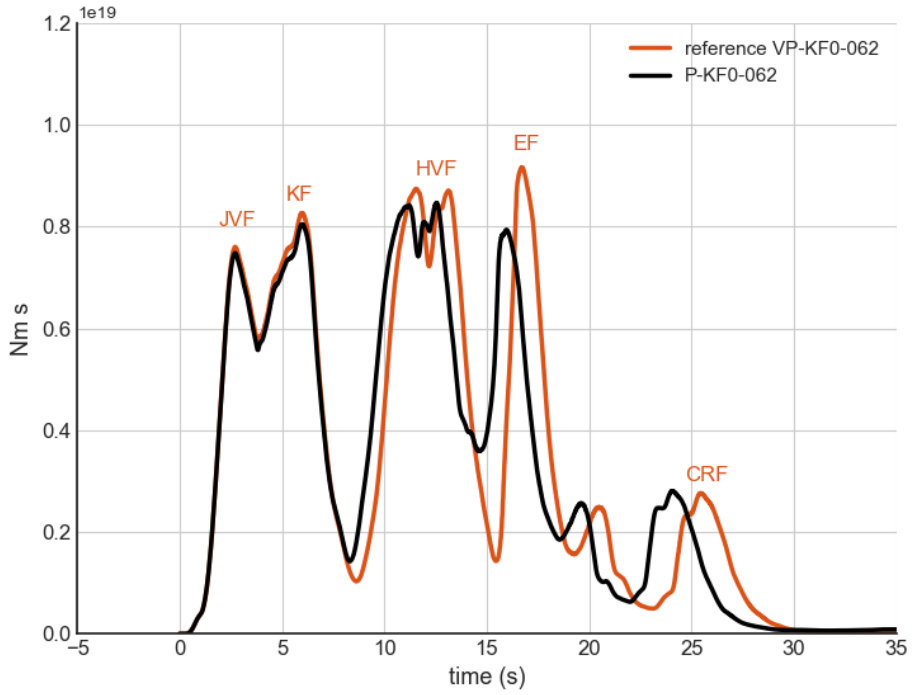

Figure 15. Seismic moment-release rate of the reference model including off-fault plasticity and viscoelastic attenuation (VP-KF0-062, orange) in comparison to the corresponding simulation accounting for off-fault plasticity but not for viscoelastic attenuation (P-KF0-062, black).

observe the lowest distance dependence of variability for the kinematic source model of *Zeng and Anderson* [2000] that has its highest slip at depth, similar to our simulations.

In contrast to the purely elastic simulation, ground motion variability close to the fault for the reference simulation with plasticity is increased by 29.4% with respect to variability between 85 km and 105 km R_{JB}-distance. Localized plastic deformation (see Fig. 10) additionally alters PGVs very heterogeneously in the vicinity of the fault, therefore further increasing the variability within the first 20 km.

We conclude that mean peak ground motions are stronger reduced in the vicinity of the fault when accounting for off-fault plastic yielding, but the reduction is still visible at 100 km R_{JB}-distance. Additionally, ground motion variability for the reference simulation using off-fault plasticity is close to what is commonly used in GMPEs [*Boore and Atkinson*, 2008], and in general lower than in the elastic simulations. Due to the heterogeneous distribution of near-fault plastic yielding, ground motion variability in the simulation with off-fault plasticity are slightly increased within 20 km to the fault.

4.4 The Effect of Attenuation on Dynamic Triggering

Viscoelastic attenuation is an important physical mechanism that describes the gradual damping of high frequency seismic waves with propagation distance. Our reference scenario accounts for viscoelastic-plastic rheology (model VP-KF0-062). We clearly observe decreasing peak velocities with increasing travel distances in comparison to a setup without attenuation (model P-KF0-062, see Fig. D.1 in Appendix D:

for synthetic PGVs of all seismic stations without and with accounting for seismic attenuation). However, as a consequence of the damping of the high frequency seismic waves, seismic attenuation also affects rupture dynamics, specifically the dynamically triggered rupture transfers and re-initiation.

We find that all rupture transfer processes of our extended fault system are affected by the energy the seismic waves carry - no attenuation meaning more seismic energy and thus facilitation of dynamic triggering. Fig. 15 shows the moment rate over time of the reference simulation (model VP-KF0-062, orange) compared to the same simulation but without accounting for seismic attenuation (model P-KF0-062, black). Within the first 8 s rupture propagation and moment rate release are identical. At 8.1 s, after the rupture delay at the HVF central fault bend, we observe faster rupture re-initiation in the simulation without attenuation. Additionally, rupture is dynamically triggered at the EF at an earlier time (at 15 s). With attenuation, rupture jumping to the CRF is additionally delayed (from 17.9 to 22 s).

The faster rupture initiation after the bend at the center of the HVF in the simulation without attenuation suggests that rupture transfer is facilitated by the non-damped arriving seismic waves. We note, that dynamic triggering in a segmented fault system is highly non-linear and may bridge distances larger than expected from simplified setups [*Harris and Day*, 1993; *Oglesby*, 2008; *Finzi and Langer*, 2012b]. For instance, at the northern most segments which are affected by seismic waves traveling more than 50 km from the hypocenter remote triggering is delayed with attenuation. Still, the resulting slip distribution and moment magnitude is in both cases identical (M_w 7.29). A detailed analysis of the frequency bands responsible for remote triggering of rupture at adjacent fault segments will be considered in future work.

For simulations without off-fault plasticity, rupture dynamics are less altered by ignoring attenuation. This suggests, that near fault plastic deformation here considerably increases the uniqueness of conditions allowing sustained rupture; as a consequence dynamic triggering, and an exact modeling of the emanated seismic wave field and its interaction with the fault system is crucial. The spatial extend of the Landers fault system leads to dynamic triggering effects over large distances, distances large enough to be affected critically by seismic attenuation.

4.5 Shallow Slip at the Camp Rock Fault

It is to-date under debate whether the shallow part of the CRF slipped co-seismically or if it was triggered by static stress changes shortly after the event [*Sieh*, 1996; *Kaneda and Rockwell*, 2009]. A lack of aftershock recordings [*Hauksson et al.*, 1993; *Sieh et al.*, 1993] as well as the asymmetric right-lateral slip pattern indicate that slip may have been induced by static stress changes due to the failure of the EF [*Sieh*, 1996; *Kaneda and Rockwell*, 2009]. Interestingly, slip inversion results based on GPS data [*Wald and Heaton*, 1994; *Hernandez et al.*, 1999; *Gombert et al.*, 2018] show higher shallow slip in the northernmost part of the fault system than inversions based on seismic recordings [*Cohee and Beroza*, 1994; *Cotton and Campillo*, 1995]. However, due to the restriction of most inversion methods to simplified fault surfaces it is difficult to assign the shallow slip non-ambiguously to either the EF and CRF.

Our dynamic rupture model of the Landers earthquake with plasticity does not create large shallow slip at the northernmost fault segment. The central part of the CRF is dynamically triggered at a depth of $\approx$ 8 km. Rupture dies out quickly when it reaches the surface, without inducing large surface slip (average surface slip along the CRF of 0.8 m). Similar values are obtained even for the corresponding elastic simulation (although the elastic SSD is lower due to a lower maximum slip at depth).

The here assumed regional stress field in conjuncture with the fault geometry at the CRF inhibits large surface slip. Dynamic rupture experiments varying stress orientations and stress amplitudes reveal that considerably higher surface slip is not possible to generate while breaking the full fault system and generating reasonable amount of slip at the the southernmost fault segments. Thus, our dynamic rupture model aligns with the hypothesis of statically triggered shallow rupture.

Kaneda and Rockwell [2009] investigate the CRF in detail by analyzing tectonic-geomorphic features along this fault segment. The 1992 rupture at the CRF differs distinctly from the characteristics of the penultimate and long-term ruptures. In particular, the vertical motion is almost opposite to previous ruptures. They conclude that the fault geometry might include a small dipping component at the center of the fault segment which shows a reverse-slip motion induced by static stress changes. In contrast, our dynamic rupture model uses a vertical fault geometry for the entire fault system. Future work could investigate whether a dipping fault geometry at the center of the CRF facilitates dynamic rupture activation and propagation at shallow depth or if shallow slip can only be induced by static stress changes.

5 Conclusions

We present a mechanically viable dynamic rupture scenario of the 1992 Landers earthquake, which sheds light on the physical mechanisms of rupture transferring between adjacent fault segments. Our model is characterized by a high degree of realism leading in turn to a high degree of uniqueness and reproduces a wide range of observations.

The model accounts for high-resolution topography, complex fault system geometries, 3D subsurface structure, viscoelastic attenuation, off-fault plasticity and depth-dependent cohesion. Earthquake rupture is able to interconnect all geometrically complex segments of the fault system under the assumption of smoothly varying fault stress and strength conditions. The simulation reproduces far-field and near-field observations, such as the total moment rate, final fault slip, seismic waveforms and respective peak ground motions, as well as off-fault deformation patterns. Our dynamic rupture earthquake scenario allows detailed analysis of the mechanical sustainability of dynamic rupture transfer with respect to the interplay of tectonic stress and local fault strength conditions.

Sustained dynamic rupture of all Landers fault segments poses a strong constraint on model parametrization. Specifically, the facilitation and timing of rupture transfers between the principal fault segments determine the amplitude and orientation of initial fault stresses and friction. Scenarios succeeding in rupture across the entire fault system feature very robust slip distribution under variation of nucleation patch sizes and frictional parameters that alter the stress drop– however timing of rupture transfers are highly sensitive.

Importantly, the resulting source dynamics depict a variety of rupture transfer mechanisms, including dynamic triggering and direct rupture branching and combination of both; both mechanisms are crucial to drive rupture across the entire fault system given the fault geometry we consider in this study. Large stress changes due to the subsequent, or almost simultaneous, failure of the HVF and EF enables dynamic triggering of the CRF over distances much larger than previously suggested.

Our dynamic rupture model reveals that dynamic triggering - often associated with the observed segmentation of moment release - is not the only feature reducing the moment release. In particular, rupture deceleration due to complex fault geometry strongly affects the moment-release rate, thus complicating the inference of rupture transfer mechanisms from observations.

In distinction to previous models [*Aochi and Fukuyama*, 2002; *Aochi et al.*, 2003], we find that a steeply oriented regional stress field (maximum principal stress close to north) is crucial to allow the northernmost part (CRF) to rupture. Interestingly, large shallow slip of the CRF is dynamically inhibited in our scenario, supporting the hypothesis of statically triggered shallow rupture at the CRF shortly after the main event [*Sieh*, 1996; *Kaneda and Rockwell*, 2009]. We find that it is impossible to generate considerably higher surface slip by variations in stress orientations and stress amplitudes while simultaneously breaking the entire fault system and creating reasonable amount of slip at the southernmost fault segments for the given fault geometry and under the assumption of frictional parameters being constant at all depths.

Rupture termination in our model is overall independent of the geometrically prescribed fault endings, with exception of the northernmost section of the HVF. Rupture is stopped smoothly corresponding to fault orientation towards the principal stress orientation. Our dynamic rupture model therefore provides a consistent explanation for spontaneous rupture termination on most of the principal fault segments, although fault structures in reality continue.

We show that an along-strike variability of the SSD of up to 20% is possible, even for laterally constant rock cohesion and bulk friction. Since these variations also exists for the purely elastic simulation, they can be attributed to different principal stress directions and the complex fault geometry. Shallow plastic deformation increases the SSD between 0.7% and 36% in dependence of the fault orientation and resulting rupture dynamics. Relatively high SSDs (up to 50%) are possible for good quality rock without the presence of pre-exising fault-damage zones if stress drop is high. We observe dramatically increased off-fault deformation in the vicinity of fault bends and intersections, in excellent agreement with recent maps of fault-zone width [*Milliner et al.*, 2015]. Good agreement of synthetic waveform characteristics and associated peak ground velocities with observations include capturing of the main S-wave pulses, amplitudes, and shaking duration.

In contrast to a purely elastic simulation, our viscoelastic-plastic scenario reduces the mean PGVs in forward direction by up to 35%, while ground motions perpendicular to the fault are very similar. Rupture transfer and moment rate of the simulation with plasticity can be partially emulated by an elastic simulation with increased critical slip distance D_c that leads to slower rupture speeds and longer delays for transferring rupture to adjacent segments. However, the elastic simulation with decreased rupture speed still overestimates PGVs in forward rupture direction by 11%.

Ground motion variability with respect to fault distance is in general lower for the simulation with off-fault plasticity, and found to be close to 0.56 [e.g., *Boore and Atkinson*, 2008], commonly assumed in GMPEs. However, the simulation accounting for plastic yielding creates higher ground motion variability close to the fault, presumably due to the heterogeneous distribution of near-fault plastic yielding.

We find that the complex source dynamics of the Landers fault system induce dynamic triggering over large distances, which are large enough to be strongly affected by seismic attenuation. The effect of attenuation on dynamic triggering is pronounced for models including off-fault plastic deformation. This suggests that our chosen model ingredients considerably increase the uniqueness of conditions allowing sustained rupture;

We demonstrate that physics-based modeling of realistically constrained, in-scale earthquake scenarios may successfully complement and augment earthquake source observations. An improved understanding of earthquake source physics can be achieved when combining various representations of natural complexities.

Appendix

A: Cohesive Zone Width

Wollherr et al. [2018] find, that the cohesive zone width can vary considerably across geometrically complex fault systems. The authors suggest that its minimum should pose the inherent length scale to be resolved instead of an average value. Additionally, a measured cohesive zone width may vary with underlying (coarse) fault discretization. Only for sufficiently high resolutions of the fault, one can determine a correct ("numerically converged") cohesive zone width. Higher resolutions need to be considered to determine whether the cohesive zone width reached a stable value (i.e. converged) or if the solution is still changing with mesh refinement.

To calculate the cohesive zone width, we determine the time of the onset of rupture (RT), as well as the time when shear stresses reach their dynamic value (DS). Using the rupture speed v_r, the cohesive zone is then defined by the formula $(DS - RT)v_r$. For our preferred model the minimum cohesive zone width is measured as 155 m located at the HVF at a depth of 8 km. For a given on-fault resolution of 200 m, the minimum cohesive zone is then resolved by 0.775 mesh elements (or 4.56 sub-elemental Gaussian integration points for polynomial degree $p = 4$.). Note, that due to the different principal stress amplitudes and orientations used in this model, the rupture paths varies from the scenarios in *Wollherr et al.* [2018] and consequently the cohesive zone width is slightly smaller than reported therein.

The convergence rates in *Wollherr et al.* [2018] help to determine the potential error level with respect to a high resolution reference solution given the minimum cohesive zone width resolution and a polynomial degree p. For $p = 4$, the 200 m on-fault resolution corresponds to a mean error of 0.16% for peak slip rate time, 4.16% for peak slip rate, 0.15% for rupture arrival and 0.94% for final slip. These values are sufficiently small to accurately resolve the source dynamics [*Day et al.*, 2005].

B: Resolved Frequencies

We analyze the distance dependent frequency content of synthetic velocity recordings to determine the maximum resolved frequency content of the wave field in our simulation. Fig. B.1 shows the normalized frequency spectrum of the observed and simulated seismic velocities for a selection of seismic stations. The stations locations are visualized in Fig. 7. Their full name, R_{JB}-distance, and corresponding Vs_{30}-value can be found in Table 2.

The highest resolved frequencies are determined by evaluating the maximum frequency for which the synthetic spectra align with the expected ω^{-1} frequency decay. In particular close to the faults, our simulation reaches very high frequencies without modeling small-scale roughness or pre-stress heterogeneities. The station LUC, which is the closest station to the fault traces (0.47 R_{JB}-distance), shows frequencies reaching up to 4.0 Hz. The stations YER (24.37 km R_{JB}-distance) in forward direction includes frequencies up to $\approx$ 3.0 Hz. With increasing distance the resolved frequency content increasingly deviate from an ideal ω^{-1} decay: Stations FRT (64.97 km R_{JB}-distance) and BOR (87.33 km R_{JB}-distance) reach up to 2.0 Hz and 1 Hz, respectively. In the low velocity basin of the Salton Sea, station SAL (102.8 km R_{JB}-distance) only resolves a maximum frequency of 1.0 Hz. Therefore, to assure consistent frequency ranges of all synthetics, we bandpass filter all stations in Sec. 3.5.2 in between 0.05 and 1.0 Hz.

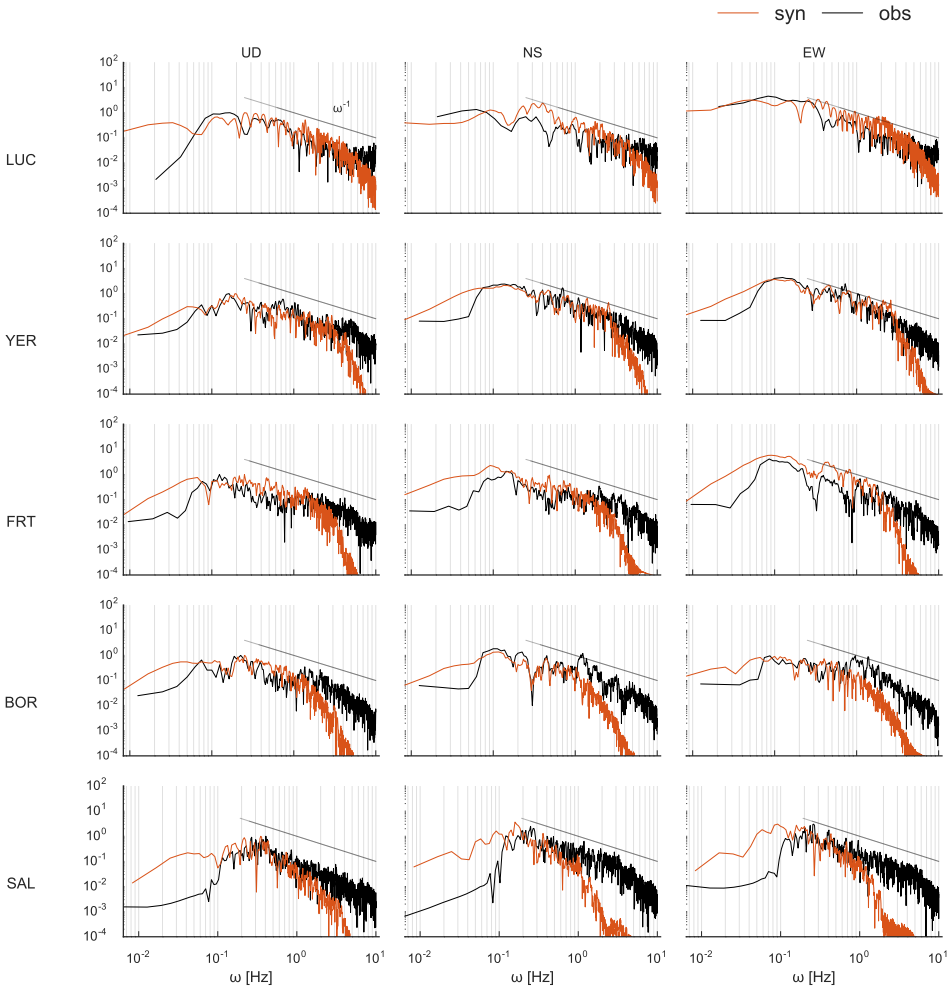

Figure B.1. Normalized frequency spectra for observed (orange) and simulated (black) seismic velocities for a selection of stations listed in Table 2. The stations are ordered by their R_{JB}-distance. The black line indicates the ideally expected frequency decay of ω^{-1}. The frequencies are cut at their respective Nyquist frequency.

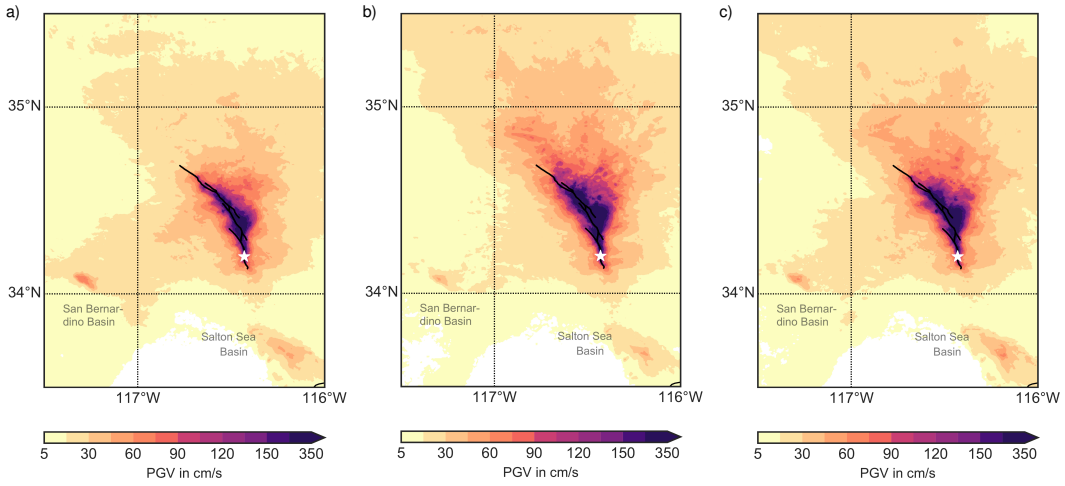

Figure C.1. Simulated GMRotD50 [*Boore et al.*, 2006] PGVs above 5 cm/s for the a) reference simulation with plasticity (VP-KF0-062), b) the corresponding purely elastic simulation (VE-KF0-062) and b) for the purely elastic simulation with increased D_c (VE-KF0-072). The white star marks the epicenter of the 1992 event.

C: Peak Ground Motions Maps

We here show a close-up of the PGVs of the three presented simulations in Sec. 4.2: the reference simulation with plasticity (Fig. C.1 a)), the corresponding elastic simulation (Fig. C.1 b)) and the corresponding elastic simulation with increased D_c (Fig. C.1 c)). Consistent with the findings for the mean PGVs with respect to the distance or azimuth bins in Sec. 4.2, we find that the directivity effect is much more pronounced in the elastic simulations. However, an increase of D_c in the elastic simulation drastically reduces the PGVs in forward direction while the PGV in the Salton Sea Basin are slightly increased due to the slower rupture which results in more backward propagating rupture. Still, ground motions in the plastic simulation differ, in particular in the forward direction.

D: Effect of Attenuation on Peak Ground Motions

We discuss in Sec. 4.4 the effect of attenuation on source dynamics, in particular on dynamic triggering. Fig. D.1 shows how attenuation affects the simulated PGVs for the stations listed in Sec. 3.5 and visualized in Fig. 7. While PGVs are almost identical for near fault stations up to 20 km R_{JB}-distance, we observe a clear decrease in PGVs for greater distances due to the attenuation of seismic waves with propagation distance.

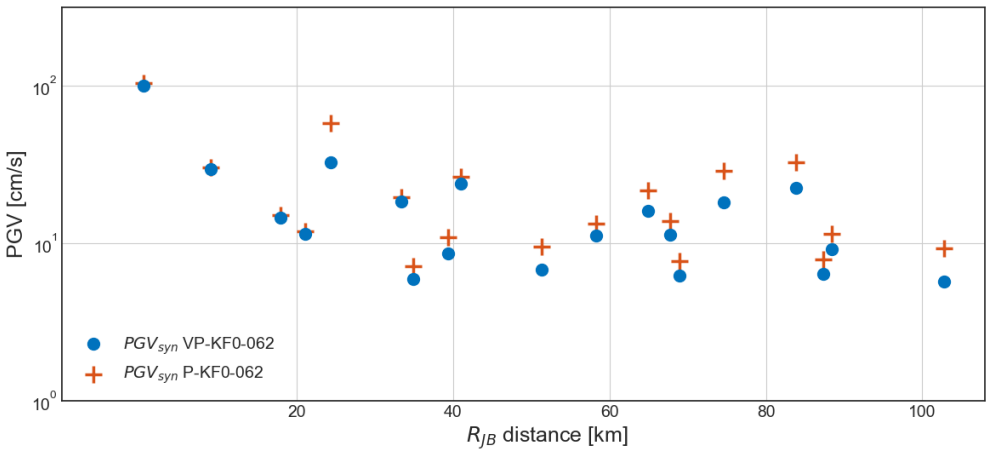

Figure D.1. Simulated PGVs with (blue circles) and without attenuation (orange crosses) in dependence of R_{JB}-distance of the stations given in Table 2.

Acknowledgments
We thank Christopher Milliner for providing the left part of Fig. 10 which is similar to Fig. 7 in *Milliner et al.* [2015]. All data used are listed in the paper. Simulation results were obtained using the open-source software package SeisSol, freely available at github.com/SeisSol/SeisSol. Computing resources were provided by the Leibniz Supercomputing Centre (LRZ, projects no. pr45fi and pr63qo on SuperMUC). The work presented in this paper was supported by the German Research Foundation (DFG) (projects no. KA 2281/4-1, GA 2465/2-1, BA 3529/6-1), by the Bavarian Competence Network for Technical and Scientific High Performance Computing (KONWIHR), project GeoPF (Geophysics for PetaFlop Computing), by the Volkswagen Foundation (project ASCETE – Advanced Simulation of Coupled Earthquake-Tsunami Events, grant No. 88479), by the European Union's Horizon 2020 research and innovation program under grant agreement No. 671698 and No. 823844 as well as by King Abdullah University of Science and Technology (KAUST) in Thuwal, Saudi Arabia, under grant ORS-2016-CRG5-3027-04 and OSR-CRG2017-3389. P. M. Mai is sponsored through KAUST research fund BAS/1339-01-01.

References

Abercrombie, R., and J. Mori (1994), Local observations of the onset of a large earthquake: 28 June 1992 Landers, California, *Bull. Seism. Soc. Am.*, *84*(3), 725.

Ampuero, J.-P., J.-P. Vilotte, and F. Sanchez-Sesma (2002), Nucleation of rupture under slip dependent friction law: simple models of fault zone, *J. Geophys. Res.*, *107*(B12).

Ando, R., K. Imanishi, Y. Panayotopoulos, and T. Kobayashi (2017), Dynamic rupture propagation on geometrically complex fault with along-strike variation of fault maturity: Insights from the 2014 Northern Nagano earthquake Crustal Dynamics, *Earth Planets Space.*, *69*(1), doi:10.1186/s40623-017-0715-2.

Andrews, D. J. (1999), Test of two methods for faulting on finite-difference calculations, *Bull. Seism. Soc. Am.*, *89*(4), 931–937.

Andrews, D. J. (2005), Rupture dynamics with energy loss outside the slip zone, *J. Geophys. Res.*, *110*(1), 1–14, doi:10.1029/2004JB003191.

Aochi, H., and E. Fukuyama (2002), Three-dimensional nonplanar simulation of the 1992 Landers earthquake, *J. Geophys. Res.*, *107*(B2), B22,035, doi:10.1029/2000JB000061.

Aochi, H., and R. Madariaga (2003), The 1999 Izmit, Turkey, earthquake: Nonplanar fault structure, dynamic rupture process, and strong ground motion, *Bull. Seism. Soc. Am.*, *93*(3), 1249–1266, doi:10.1785/0120020167.

Aochi, H., R. Madariaga, and E. Fukuyama (2003), Constraint of fault parameters inferred from nonplanar fault modeling, *Geochem. Geophys. Geosyst.*, *4*(2), 1–16, doi:10.1029/2001GC000207.

Barall, M. (2009), A grid-doubling finite-element technique for calculating dynamic three-dimensional spontaneous rupture on an earthquake fault, *Geophys. J. Int.*, *178*(2), 845–859, doi:10.1111/j.1365-246X.2009.04190.x.

Bhat, H. S., M. Olives, R. Dmowska, and J. R. Rice (2007), Role of fault branches in earthquake rupture dynamics, *J. Geophys. Res.*, *112*(B11), B11,309, doi:10.1029/2007JB005027.

Bizzarri, A. (2010), How to promote earthquake ruptures: Different nucleation strategies in a dynamic model with slip-weakening friction, *Bull. Seism. Soc. Am.*, *100*(3), 923–940.

Bommer, J. J., and N. A. Abrahamson (2006), Why do modern probabilistic seismic-hazard analyses often lead to increased hazard estimates?, *Bull. Seism. Soc. Am.*, *96*(6), 1967–1977.

Boore, D. M., and G. M. Atkinson (2008), Ground-motion prediction equations for the average horizontal component of PGA, PGV, and 5%-damped PSA at spectral periods between 0.01 s and 10.0 s, *Earth. Spectra*, *24*(1), 99–138.

Boore, D. M., J. Watson-Lamprey, and N. A. Abrahamson (2006), Orientation-independent measures of ground motion, *Bull. Seism. Soc. Am.*, *96*(4A), 1502–1511.

Bouchon, M., and M. Campillo (1998), Stress field associated with the rupture of the 1992 Landers, California, earthquake and its implifications concerning the fault strength at the onset of the earthquake, *J. Geophys. Res.*, *103*(B9), 21,091–21,097.

Breuer, A., A. Heinecke, S. Rettenberger, M. Bader, A.-A. Gabriel, and C. Pelties (2014), Sustained Petascale Performance of Seismic Simulations with SeisSol on SuperMUC, in *Proceedings of the International Supercomputing Conference*, pp. 1–18, Springer International Publishing, Cham.

Breuer, A., A. Heinecke, L. Rannabauer, and M. Bader (2015), High-Order ADER-DG Minimizes Energy-and Time-to-Solution of SeisSol, in *Proceedings of the International Conference on High Performance Computing*, pp. 340–357, Springer International Publishing, Cham.

Breuer, A., A. Heinecke, and M. Bader (2016), Petascale local time stepping for the ADER-DG finite element method, in *2016 IEEE International Parallel and Distributed Processing Symposium*, pp. 854–863, IEEE.

Campbell, K. W., and Y. Bozorgnia (1994), Empirical analysis of strong ground motion from the 1992 Landers, California, earthquake, *Bull. Seism. Soc. Am.*, *84*(3), 573.

Campillo, M., and R. J. Archuleta (1993), A rupture model for the 28 June 1992 Landers, California, earthquake, *Geophys. Res. Lett.*, *20*(8), 647–650.

Candela, T., F. Renard, Y. Klinger, K. Mair, J. Schmittbuhl, and E. E. Brodsky (2012), Roughness of fault surfaces over nine decades of length scales, *J. Geophys. Res.*, *117*(B8), doi:10.1029/2011JB009041.

Chen, X. (1995), Near-field ground motion from the Landers earthquake, Ph.D. thesis, California Institute of Technology.

Cohee, B. P., and G. C. Beroza (1994), Slip distribution of the 1992 Landers earthquake and its implications for earthquake source mechanics, *Bull. Seism. Soc. Am.*, *84*(3), 692–712, doi:10.1016/0148-9062(95)94486-9.

Cotton, F., and M. Campillo (1995), Frequency domain inversion of strong motions: Application to the 1992 Landers earthquake, *J. Geophys. Res.*, *100*(B3), 3961–3975.

Dalguer, L. A., and S. M. Day (2007), Staggered-grid split-node method for spontaneous rupture simulation, *J. Geophys. Res.*, *112*(2), 1–15, doi:10.1029/2006JB004467.

Das, S., and K. Aki (1977), Fault plane with barriers: a versatile earthquake model, *J. Geophys. Res.*, *82*(36), 5658–5670.

Day, S. M., L. A. Dalguer, N. Lapusta, and Y. Liu (2005), Comparison of finite difference and boundary integral solutions to three-dimensional spontaneous rupture, *J. Geophys. Res.*, *110*(B12), doi:10.1029/2005JB003813, b12307.

De la Puente, J., J.-P. Ampuero, and M. Käser (2009), Dynamic rupture modeling on unstructured meshes using a discontinuous Galerkin method, *J. Geophys. Res.*, *114*(B10), b10302.

DeDontney, N., J. R. Rice, and R. Dmowska (2012), Finite Element Modeling of Branched Ruptures Including Off-Fault Plasticity, *Bull. Seism. Soc. Am.*, *102*(2), 541–562, doi:10.1785/0120110134.

Dibblee, T. W. J. (1967), Geologic Map of the Old Woman Springs Quadrangle San Bernardino County, California, *Tech. rep.*, Department of the Interior United States Gelogical Survey.

Dokka, R. K., and C. J. Travis (1990), Late Cenozoic strike-slip faulting in the Mojave Desert, California, *Tectonics*, *9*(2), 311–340.

Dreger, D. S. (1994), Investigation of the Rupture Process of the 28 June 1992 Landers Earthquake Utilizing Terrascope, *Bull. Seism. Soc. Am.*, *84*(3), 713–724.

Dumbser, M., and M. Käser (2006), An arbitrary high-order discontinuous Galerkin method for elastic waves on unstructured meshes II. The three-dimensional isotropic case, *Geophys. J. Int.*, *167*(1), 319–336, doi:10.1111/j.1365-246X.2006.03120.x.

Dunham, E. M. (2007), Conditions governing the occurrence of supershear ruptures under slip-weakening friction, *J. Geophys. Res.*, *112*(7), 1–24, doi:10.1029/2006JB004717.

Dunham, E. M., D. Belanger, L. Cong, and J. E. Kozdon (2011a), Earthquake Ruptures with Strongly Rate-Weakening Friction and Off-Fault Plasticity, Part 2: Nonplanar Faults, *Bull. Seism. Soc. Am.*, *101*(5), 2308–2322, doi:10.1785/0120100076.

Dunham, E. M., D. Belanger, L. Cong, and J. E. Kozdon (2011b), Earthquake Ruptures with Strongly Rate-Weakening Friction and Off-Fault Plasticity, Part 1: Planar Faults, *Bull. Seism. Soc. Am.*, *101*(5), 2296–2307, doi:10.1785/0120100075.

Duru, K., and E. M. Dunham (2016), Dynamic earthquake rupture simulations on nonplanar faults embedded in 3D geometrically complex, heterogeneous elastic solids, *J. Comp. Phys.*, *305*, 185–207.

Ely, G. P., S. M. Day, and J.-B. Minster (2008), A support-operator method for viscoelastic wave modelling in 3-D heterogeneous media, *Geophys. J. Int.*, *172*(1), 331–344.

Emerson Paradigm Holding (2018), GoCad: A computer aided design program for geological applications, `http://www.pdgm.com/products/gocad/`.

Farr, T. G., P. A. Rosen, E. Caro, R. Crippen, R. Duren, S. Hensley, M. Kobrick, M. Paller, E. Rodriguez, L. Roth, D. Seal, S. Shaffer, J. Shimada, J. Umland, M. Werner, M. Oskin, D. Burbank, and D. Alsdorf (2007), The Shuttle Radar Topography Mission, *Rev. Geophys.*, *45*(2), doi:10.1029/2005RG000183.

Faulkner, D. R., T. M. Mitchell, E. Jensen, and J. Cembrano (2011), Scaling of fault damage zones with displacement and the implications for fault growth processes, *J. Geophys. Res.*, *116*(B5), doi:10.1029/2010JB007788.

Fialko, Y. (2004a), Probing the mechanical properties of seismically active crust with space geodesy: Study of the coseismic deformation due to the 1992 Mw 7.3 Landers (southern California) earthquake, *J. Geophys. Res.*, *109*(B3), B03,307, doi:10.1029/2003JB002756.

Fialko, Y. (2004b), Evidence of fluid-filled upper crust from observations of postseismic deformation due to the 1992 Mw 7.3 Landers earthquake, *J. Geophys. Res.*, *109*(8), 1–17, doi:10.1029/2004JB002985.

Fialko, Y., D. Sandwell, M. Simons, and P. Rosen (2005), Three-dimensional deformation caused by the Bam, Iran, earthquake and the origin of shallow slip deficit, *Nature*, *435*(7040), 295–299, doi:10.1038/nature03425.

Finzi, Y., and S. Langer (2012a), Damage in step-overs may enable large cascading earthquakes, *Geophys. Res. Lett.*, *39*(May), 1–5, doi:10.1029/2012GL052436.

Finzi, Y., and S. Langer (2012b), Predicting rupture arrests, rupture jumps and cascading earthquakes, *J. Geophys. Res.*, *117*(12), 1–11, doi:10.1029/2012JB009544.

Fleming, R., J. Messerich, and K. Cruikshank (1998), Fractures along a portion of the Emerson fault zone related to the 1992 Landers, California, earthquake: Evidence for the rotation of the Galway-Lake-Road block, *Geol. Soc. Am., Map and Chart Series*, mCH082.

Fliss, S., H. S. Bhat, R. Dmowska, and J. R. Rice (2005), Fault branching and rupture directivity, *J. Geophys. Res.*, *110*(B6), B06,312, doi:10.1029/2004JB003368.

Freymueller, J., N. E. King, and P. Segall (1994), The co-seismic slip distribution of the Landers earthquake, *Bull. Seism. Soc. Am.*, *84*(3), 646–659.

Gabriel, A., J. Ampuero, L. A. Dalguer, and P. M. Mai (2012), The transition of dynamic rupture styles in elastic media under velocity-weakening friction, *J. Geophys. Res.*, *117*(B9), doi:10.1029/2012JB009468.

Gabriel, A.-A., J.-P. Ampuero, L. A. Dalguer, and P. M. Mai (2013), Source properties of dynamic rupture pulses with off-fault plasticity, *J. Geophys. Res.*, *118*(8), 4117–

4126, doi:10.1002/jgrb.50213.

Galis, M., C. Pelties, J. Kristek, P. Moczo, J.-P. Ampuero, and P. M. Mai (2014), On the initiation of sustained slip-weakening ruptures by localized stresses, *Geophys. J. Int.*, *200*(2), 890–909, doi:10.1093/gji/ggu436.

Gombert, B., Z. Duputel, R. Jolivet, C. Doubre, L. Rivera, and M. Simons (2018), Revisiting the 1992 Landers earthquake: a Bayesian exploration of co-seismic slip and off-fault damage, *Geophys. J. Int.*, *212*(2), 839–852, doi:10.1093/gji/ggx455.

Graizer, V. M. (2005), Effect of tilt on strong motion data processing, *Soil Dyn. Earth. Eng.*, *25*(3), 197–204.

Graves, R. W., and A. Pitarka (2010), Broadband Ground-Motion Simulation Using a Hybrid Approach, *Bull. Seism. Soc. Am.*, *100*(5A), 2095–2123, doi:10.1785/0120100057.

Graves, R. W., B. T. Aagaard, K. W. Hudnut, L. M. Star, J. P. Stewart, and T. H. Jordan (2008), Broadband simulations for Mw 7.8 southern San Andreas earthquakes: Ground motion sensitivity to rupture speed, *Geophys. Res. Lett.*, *35*(22), doi:10.1029/2008GL035750.

Gross, S., and C. Kisslinger (1997), Estimating tectonic stress rate and state with Landers aftershocks, *J. Geophys. Res.*, *102*(B4), 7603, doi:10.1029/96JB03741.

Harris, R., and S. M. Day (1993), Dynamic of fault interaction: parallel strike-slip faults, *J. Geophys. Res.*, *98*(No. B3), 4461–4472, doi:10.1029/92JB02272.

Harris, R. A., M. Barall, B. Aagaard, S. Ma, D. Roten, K. Olsen, B. Duan, D. Liu, B. Luo, K. Bai, J. Ampuero, Y. Kaneko, A. Gabriel, K. Duru, T. Ulrich, S. Wollherr, Z. Shi, E. Dunham, S. Bydlon, Z. Zhang, X. Chen, S. N. Somala, C. Pelties, J. Tago, V. M. CruzAtienza, J. Kozdon, E. Daub, K. Aslam, Y. Kase, K. Withers, and L. Dalguer (2018), A Suite of Exercises for Verifying Dynamic Earthquake Rupture Codes, *Seismol. Res. Lett.*, *89*(3), 1146, doi:10.1785/0220170222.

Hauksson, E. (1994), State of stress from focal mechanisms before and after the 1992 Landers earthquake sequence, *Bull. Seism. Soc. Am.*, *84*(3), 917–934, doi:10.1016/0148-9062(95)94483-4.

Hauksson, E., L. M. Jones, K. Hutton, and D. Eberhart-Phillips (1993), The 1992 Landers earthquake sequence: Seismological observations, *J. Geophys. Res.*, *98*(B11), 19,835–19,858.

Heinecke, A., A. Breuer, S. Rettenberger, M. Bader, A.-A. Gabriel, C. Pelties, A. Bode, W. Barth, and X.-K. Liao (2014), Petascale High Order Dynamic Rupture Earthquake Simulations on Heterogeneous Supercomputers, in *Proceedings of the International Conference for High Performance Computing, Networking, Storage and Analysis*, pp. 3–15, IEEE, doi:10.1109/SC.2014.6.

Hernandez, B., F. Cotton, and M. Campillo (1999), Contribution of radar interferometry to a two-step inversion of the kinematic process of the 1992 Landers earthquake, *J. Geophys. Res.*, *104*(B6), 13,083–13,099.

Hill, R., J. Treiman, J. Given, J. Pechman, J. McMillan, and J. Ebel (1980), Geologic study of the Homestead Valley earthquake swarm of March 15, 1979, *California Geology*, *33*(3), 60–67.

Ida, Y. (1972), Cohesive Force across the Tip of a Longitudinal-Shear Crack and Griffith's Specific Surface Energy, *J. Geophys. Res.*, *77*(20), 3796–3805.

Imperatori, W., and P. M. Mai (2015), The role of topography and lateral velocity heterogeneiteis on near-source scattering and ground-motion variability, *Geophys. J. Int.*, *202*, 2163–2181, doi:10.1093/gji/ggv281.

Kagan, Y. Y., and H. Houston (2005), Relation between mainshock rupture process and Omori's law for aftershock moment release rate, *Geophys. J. Int.*, *163*(September), 1039–1048, doi:10.1111/j.1365-246X.2005.02772.x.

Kanamori, H., and L. Rivera (2006), Energy Partitioning During an Earthquake, in *Earthquakes: Radiated Energy and the Physics of Faulting Geophysical Monograph Series 170*, pp. 3–13, American Geophysical Union.

Kanamori, H., H.-K. Thio, D. Dreger, E. Hauksson, and T. Heaton (1992), Initial investigation of the Landers, California, earthquake of 28 June 1992 using TERRAscope, *Geophys. Res. Lett.*, *19*(22), 2267–2270.

Kaneda, H., and T. K. Rockwell (2009), Triggered and primary surface ruptures along the camp rock fault, eastern California shear zone, *Bull. Seism. Soc. Am.*, *99*(5), 2704–2720, doi:10.1785/0120080310.

Kaneko, Y., and Y. Fialko (2011), Shallow slip deficit due to large strike-slip earthquakes in dynamic rupture simulations with elasto-plastic off-fault response, *Geophys. J. Int.*, *186*(3), 1389–1403.

Kaneko, Y., and P. M. Shearer (2015), Variability of seismic source spectra, estimated stress drop, and radiated energy, derived from cohesive-zone models of symmetrical and asymmetrical circular and elliptical ruptures, *Journal of Geophysical Research: Solid Earth*, *120*(2), 1053–1079, doi:10.1002/2014JB011642.

Käser, M., and M. Dumbser (2006), An Arbitrary High Order Discontinuous Galerkin Method for Elastic Waves on Unstructured Meshes I: The Two-Dimensional Isotropic Case with External Source Terms, *Geophys. J. Int.*, *166*(2), 855–877.

Käser, M., V. Hermann, and J. de la Puente (2008), Quantitative accuracy analysis of the discontinuous Galerkin method for seismic wave propagation, *Geophys. J. Int.*, *173*(3), 990–999.

Kaven, J. O., and D. D. Pollard (2013), Geometry of crustal faults: Identification from seismicity and implications for slip and stress transfer models, *J. Geophys. Res.*, *118*(9), 5058–5070, doi:10.1002/jgrb.50356.

Krischer, L., T. Megies, R. Barsch, M. Beyreuther, T. Lecocq, C. Caudron, and J. Wassermann (2015), ObsPy: A Bridge for Seismology into the Scientific Python Ecosystem, *Computational Science & Discovery*, *8*(1), 014,003, doi:10.1088/1749-4699/8/1/014003.

Kristeková, M., J. Kristek, and P. Moczo (2009), Time-frequency misfit and goodness-of-fit criteria for quantitative comparison of time signals, *Geophysical Journal International*, *178*(2), 813–825, doi:10.1111/j.1365-246X.2009.04177.x.

Li, Y.-G., K. Aki, D. Adams, A. Hasemi, and W. H. K. Lee (1994a), Seismic guided waves trapped in the fault zone of the Landers, California, earthquake of 1992, *J. Geophys. Res.*, *99*(94), 11,705–11,722, doi:10.1029/94JB00464.

Li, Y.-G., K. Aki, J. E. Vidale, W. H. Lee, and C. J. Marone (1994b), Fine structure of the Landers fault zone: segmentation and the rupture process, *Science*, *265*(5170), 367–370.

Liu, J., K. Sieh, and E. Hauksson (2003), A structural interpretation of the aftershock cloud of the 1992 M w 7.3 Landers earthquake, *Bull. Seism. Soc. Am.*, *93*(3), 1333–1344.

Lozos, J. C., D. D. Oglesby, B. Duan, and S. G. Wesnousky (2011), The effects of double fault bends on rupture propagation: A geometrical parameter study, *Bull. Seism. Soc. Am.*, *101*(1), 385–398, doi:10.1785/0120100029.

Ma, S. (2008), A physical model for widespread near-surface and fault zone damage induced by earthquakes, *Geochem. Geophys. Geosyst.*, *9*(11), 1–9, doi:10.1029/2008GC002231.

Ma, S., and R. J. Archuleta (2006), Radiated seismic energy based on dynamic rupture models of faulting, *Journal of Geophysical Research: Solid Earth*, *111*(5), 1–17, doi:10.1029/2005JB004055.

Madden, E. H., and D. D. Pollard (2012), Integration of surface slip and aftershocks to constrain the 3D structure of faults involved in the M 7.3 Landers earthquake, Southern California, *Bull. Seism. Soc. Am.*, *102*(1), 321–342, doi:10.1785/0120110073.

Madden, E. H., F. Maerten, and D. D. Pollard (2013), Mechanics of nonplanar faults at extensional steps with application to the 1992 M 7.3 Landers, California, earthquake, *J. Geophys. Res.*, *118*(1), 3249–3263, doi:10.1002/jgrb.50237.

Mai, P. M., D. Schorlemmer, M. Page, J.-P. Ampuero, K. Asano, M. Causse, S. Custodio, W. Fan, G. Festa, M. Galis, et al. (2016), The earthquake-source inversion validation (SIV) project, *Seismol. Res. Lett.*, *87*(3), 690–708.

Mai, P. M., M. Galis, K. K. Thingbaijam, J. C. Vyas, and E. M. Dunham (2017), Accounting for fault roughness in pseudo-dynamic ground-motion simulations, *Pure Appl. Geophys.*, *174*(9), 3419–3450.

Milliner, C. W. D., J. F. Dolan, J. Hollingsworth, S. Leprince, F. Ayoub, and C. G. Sammis (2015), Quantifying near-field and off-fault deformation patterns of the 1992 M_w 7.3 Landers earthquake, *Geochem. Geophys. Geosyst.*, *16*, 1577–1598, doi:10.1002/2014GC005693.

Milliner, C. W. D., J. F. Dolan, J. Hollingsworth, S. Leprince, and F. Ayoub (2016), Comparison of coseismic near-field and off-fault surface deformation patterns of the 1992 Mw 7.3 Landers and 1999 Mw 7.1 Hector Mine earthquakes: Implications for controls on the distribution of surface strain, *Geophysical Research Letters*, *43*, 1–10, doi:10.1002/2016GL069841.Received.

Nur, A., H. Ron, and O. Scotti (1989), Kinematics and mechanics of tectonic block rotations, *Slow Deformation and Transmission of Stress in the Earth, AGU Geophysical Monographs*, pp. 31–46.

Oglesby, D. (2008), Rupture Termination and Jump on Parallel Offset Faults, *Bull. Seism. Soc. Am.*, *98*(1), 440–447, doi:10.1785/0120070163.

Oglesby, D. D., and P. M. Mai (2012), Fault geometry, rupture dynamics and ground motion from potential earthquakes on the North Anatolian Fault under the Sea of Marmara, *Geophys. J. Int.*, *188*(3), 1071–1087, doi:10.1111/j.1365-246X.2011.05289.x.

Olsen, K. B., R. Madariaga, and R. J. Archuleta (1997), Three-dimensional dynamic simulation of the 1992 landers earthquake, *Science*, *278*(5339), 834–838, doi:10.1126/science.278.5339.834.

Pelties, C., J. de la Puente, J.-P. Ampuero, G. B. Brietzke, and M. Käser (2012), Three-dimensional dynamic rupture simulation with a high-order discontinuous Galerkin method on unstructured tetrahedral meshes, *J. Geophys. Res.*, *117*(B2), B02,309, doi:10.1029/2011JB008857.

Pelties, C., A.-A. Gabriel, and J.-P. Ampuero (2014), Verification of an ADER-DG method for complex dynamic rupture problems, *Geosci. Model Dev.*, *7*(3), 847–866, doi:10.5194/gmd-7-847-2014,10.5194/gmdd-6-5981-2013.

Peyrat, S., K. B. Olsen, and R. Madariaga (2001), Dynamic modeling of the 1992 Landers earthquake, *J. Geophys. Res.*, *106*(B11), 26,467–26,482.

Ramirez-Guzman, L., R. W. Graves, K. B. Olsen, O. S. Boyd, C. Cramer, S. Hartzell, S. Ni, P. Somerville, R. A. Williams, and J. Zhong (2015), Ground-motion simulations of 1811–1812 New Madrid earthquakes, central United States, *Bull. Seism. Soc. Am.*, *105*(4), 1961–1988.

Restrepo-Velez, L. F., and J. J. Bommer (2003), An exploration of the nature of the scatter in ground-motion prediction equations and the implications for seismic hazard assessment, *J. Earth. Eng.*, *7*, 171–199.

Rettenberger, S., and M. Bader (2015), Optimizing Large Scale I/O for Petascale Seismic Simulations on Unstructured Meshes, in *Proceedings of the International Conference on Cluster Computing*, pp. 314–317, IEEE, Chicago, IL.

Rettenberger, S., O. Meister, M. Bader, and A.-A. Gabriel (2016), ASAGI: A Parallel Server for Adaptive Geoinformation, in *Proceedings of the Exascale Applications and Software Conference 2016*, EASC '16, pp. 2:1–2:9, ACM, New York, doi:10.1145/2938615.2938618.

Rice, J. R., C. G. Sammis, and R. Parsons (2005), Off-fault secondary failure induced by a dynamic slip pulse, *Bull. Seism. Soc. Am.*, *95*(1), 109–134.

Ripperger, J., and P. M. Mai (2004), Fast computation of static stress changes on 2D faults from final slip distributions, *Geophys. Res. Lett.*, *31*(18).

Rockwell, T. K., S. Lindvall, M. Herzberg, D. Murbach, T. Dawson, and G. Berger (2000), Paleoseismology of the Johnson Valley, Kickapoo, and Homestead Valley faults: Clustering of earthquakes in the eastern California shear zone, *Bull. Seism. Soc. Am.*, *90*(5), 1200–1236.

Roten, D., K. B. Olsen, S. M. Day, Y. Cui, and D. Fäh (2014), Expected seismic shaking in Los Angeles reduced by San Andreas fault zone plasticity, *Geophys. Res. Lett.*, *41*(8), 2769–2777, doi:10.1002/2014GL059411.

Roten, D., K. B. Olsen, Y. Cui, and S. M. Day (2015), Quantification of fault zone plasticity effects with spontaneous rupture simulations, in *Best Practices in Physics-based Fault Rupture Models for Seismic Hazard Assessment of Nuclear Installations*, Vienna, Austria.

Roten, D., Y. Cui, K. B. Olsen, S. M. Day, K. Withers, W. H. Savran, P. Wang, and D. Mu (2016), High-frequency nonlinear earthquake simulations on petascale heterogeneous supercomputers, in *Proceedings of the International Conference for High Performance Computing, Networking, Storage and Analysis*, pp. 82:1–82:12, IEEE.

Roten, D., K. B. Olsen, and S. M. Day (2017), Off-fault Deformations and Shallow Slip Deficit from Dynamic Rupture Simulations with Fault Zone Plasticity, *Geophys. Res. Lett.*, pp. 7733–7742, doi:10.1002/2017GL074323.

Sauber, J., W. Thatcher, and S. C. Solomon (1986), Geodetic measurement of deformation in the central Mojave Desert, California, *J. Geophys. Res.*, *91*(B12), 12,683–12,693.

Shaw, J. H., A. Plesch, C. Tape, M. P. Suess, T. H. Jordan, G. Ely, E. Hauksson, J. Tromp, T. Tanimoto, R. Graves, K. Olsen, C. Nicholson, P. J. Maechling, C. Rivero, P. Lovely, C. M. Brankman, and J. Munster (2015), Unified Structural Representation of the southern California crust and upper mantle, *Earth Planet. Sci. Lett.*, *415*, 1–15, doi:10.1016/j.epsl.2015.01.016.

Shi, Z., and S. M. Day (2013), Rupture dynamics and ground motion from 3D rough-fault simulations, *J. Geophys. Res.*, *118*(3), 1122–1141, doi:10.1002/jgrb.50094.

Sieh, K. (1996), The repetition of large-earthquake ruptures., *Proceedings of the National Academy of Sciences: "Earthquake Prediction: The Scientific Challenge"*, *93*(9), 3764–3771, doi:10.1073/pnas.93.9.3764.

Sieh, K., L. Jones, E. Hauksson, K. Hudnut, D. Eberhart-Phillips, T. Heaton, S. Hough, K. Hutton, H. Kanamori, A. Lilje, et al. (1993), Near-field investigations of the Landers earthquake sequence, April to July 1992, *Science*, *260*(5105), 171–176.

Simmetrix Inc. (2017), SimModeler: Simulation Modeling Suite 11.0 Documentation, *Tech. rep.*, `www.simmetrix.org`.

Sleep, N. H. (2012), Site Resonance from Strong Ground Motions at Lucerne, California, during the 1992 Landers Mainshock, *Bull. Seism. Soc. Am.*, *102*(4), 1505, doi:10.1785/0120110267.

Sowers, J. M., J. R. Unruh, W. R. Lettis, and T. D. Rubin (1994), Relationship of the Kickapoo Fault to the Johnson Valley and Homestead Valley Faults, San Bernardino County, California, *Bull. Seism. Soc. Am.*, *84*(3), 528–536.

Spotila, J. A., and K. Sieh (1995), Geological investigation of a slip gap in the surficial ruptures of the 1992 Landers earthquake, southern California, *J. Geophys. Res.*, *100*(94), 543–559.

Spudich, P., and B. S. Chiou (2008), Directivity in NGA earthquake ground motions: Analysis using isochrone theory, *Earthquake Spectra*, *24*(1), 279–298.

Strasser, F. O., N. A. Abrahamson, and J. J. Bommer (2009), Sigma: Issues, insights, and challenges, *Seismol. Res. Lett.*, *80*(1), 40–56.

Suppe, J. (1985), *Principles of structural geology*, Prentice Hall.

Tago, J., V. M. Cruz-Atienza, J. Virieux, V. Etienne, and F. J. Sánchez-Sesma (2012), A 3D hp-adaptive discontinuous Galerkin method for modeling earthquake dynamics, *J. Geophys. Res.*, *117*(3), 1–21, doi:10.1029/2012JB009313.

Ulrich, T., A.-A. Gabriel, J.-P. Ampuero, and W. Xu (2018), Dynamic viability of the 2016 Mw 7.8 Kaikura earthquake cascade on weak crustal faults, *submitted to Nature Communications*.

Unruh, J. R., W. R. Lettis, and J. M. Sowers (1994), Kinematic Interpretation of the 1992 Landers Earthquake, *Bull. Seism. Soc. Am.*, *84*(3), 537–546.

Uphoff, C., and M. Bader (2016), Generating high performance matrix kernels for earthquake simulations with viscoelastic attenuation, in *Proceedings of the 2016 International Conference on High Performance Computing and Simulation*, pp. 908–916, IEEE.

Uphoff, C., S. Rettenberger, M. Bader, E. H. Madden, T. Ulrich, S. Wollherr, and A.-A. Gabriel (2017), Extreme scale multi-physics simulations of the tsunamigenic 2004 sumatra megathrust earthquake, in *Proceedings of the International Conference for High Performance Computing, Networking, Storage and Analysis*, p. 21, ACM.

Vallée, M., and V. Douet (2016), A new database of source time functions (STFs) extracted from the SCARDEC method, *Phys. Earth Planet. Inter.*, *257*, 149–157.

Venkataraman, A., and H. Kanamori (2004), Observational constraints on the fracture energy of subduction zone earthquakes, *Journal of Geophysical Research: Solid Earth*, *109*(B5).

Vyas, J. C., P. M. Mai, and M. Galis (2016), Distance and azimuthal dependence of ground-motion variability for unilateral strike-slip ruptures, *Bull. Seism. Soc. Am.*, *106*(4), 1584–1599, doi:10.1785/0120150298.

Wald, D. J., and T. H. Heaton (1994), Spatial and Temporal Distribution of Slip for the 1992 Landers, California, Earthquake, *Bull. Seism. Soc. Am.*, *84*(3), 668–691.

Wenk, S., C. Pelties, H. Igel, and M. Käser (2013), Regional wave propagation using the discontinuous Galerkin method, *J. Geophys. Res.*, *4*(1), 43–57, doi:10.5194/se-4-43-2013.

Wesnousky, S. G. (2006), Predicting the endpoints of earthquake ruptures, *Nature*, *444*(7117), 358–360.

Wollherr, S., A.-A. Gabriel, and C. Uphoff (2018), Off-fault plasticity in three-dimensional dynamic rupture simulations using a modal Discontinuous Galerkin method on unstructured meshes: implementation, verification and application, *Geophys. J. Int.*, *214*(3), 1556–1584, doi:10.1093/gji/ggy213.

Xu, X., X. Tong, D. T. Sandwell, C. W. D. Milliner, J. F. Dolan, J. Hollingsworth, S. Leprince, and F. Ayoub (2016), Refining the shallow slip deficit, *Geophys. J. Int.*, *204*(3), 1867–1886, doi:10.1093/gji/ggv563.

Zeng, Y., and J. G. Anderson (2000), *Evaluation of numerical procedures for simulating near-fault long-period ground motions using Zeng method*, Pacific Earthquake Engineering Research Center.

Zielke, O., M. Galis, and P. M. Mai (2017), Fault roughness and strength heterogeneity control earthquake size and stress drop, *Geophys. Res. Lett.*, *44*(2), 777–783, doi:10.1002/2016GL071700.

Zinke, R., J. Hollingsworth, and J. F. Dolan (), Surface slip and off-fault deformation patterns in the 2013 mw 7.7 balochistan, pakistan earthquake: Implications for controls on the distribution of near-surface coseismic slip, *Geochemistry, Geophysics, Geosystems*, *15*(12), 5034–5050, doi:10.1002/2014GC005538.